CENTRO DE INVESTIGACIONES
EN OPTICA, A.C.

“MEDICAL APPLICATIONS OF TERAHERTZ RADIATION”

A thesis to obtain the degree of Doctor of Science (Optics) by

Goretti Guadalupe Hernández Cardoso

Advisor: Dr. Enrique Castro Camus

León · Guanajuato · México
December 2020

Abstract

Diabetic foot syndrome, a long term consequence of diabetes mellitus, is the most common cause of non-traumatic amputations. Around 8% of the world population suffers diabetes, 15% of diabetic patients present a diabetic foot ulcer which leads to amputation in 2.5% of the cases. Currently, there is no objective method for the detection of diabetic foot syndrome in its early stages. Terahertz radiation is a highly sensitive, non-invasive, non-contact probe of the water content of materials. Assuming the dehydration of the skin in the feet of diabetic patients as a central element of their deterioration process, in this thesis, Moisture MApping by Terahertz (MMAT) is proposed as a technique for the evaluation of the diabetic foot deterioration as an early diagnostic test. The image acquisition and data processing of the MMAT technique is presented together with a first clinical trial and the diagnostic potential analysis for this technique demonstrating that MMAT is a promising diagnostic technique.

The Effective Medium Theory (EMT), commonly used in the terahertz regime for the signal processing in order to quantify water in biological tissue, is a key element for the skin hydration evaluation of the MMAT technique. A comparative analysis of three EMT models, namely Maxwell-Garnett, Bruggeman and Landau-Lifshitz-Looyenga, for the determination of water content in biological tissues from terahertz spectroscopic measurements is also provided in this work. Binary controllable mixtures of biological tissues with different water content were prepared. Optical properties of the mixtures were obtained using terahertz time-domain spectroscopy. A quantitative analysis is provided by calculating the error between experimental and theoretical data determined by the EMT models, as well as by using least squares adjustments of the experimental data by the three models concluding that the Landau-Lifshitz-Looyenga and Bruggeman theories are the more suitable for modeling biological tissues in the terahertz regime.

A mis papás Lupita y César

A mis hermanos Pablo, Marycarmen y Alejandra

List of Publications

Articles

- G. G. Hernandez-Cardoso, A. K. Singh, and E. Castro-Camus, "Empirical comparison between effective medium theory models for the dielectric response of biological tissue at terahertz frequencies", *Applied Optics*, (2020).

- G. G. Hernandez-Cardoso, S. C. Rojas-Landeros, M. Alfaro-Gomez, I. Salas-Gutierrez, and E. Castro-Camus, "Pixel statistical analysis of diabetic vs. non-diabetic foot-sole spectral terahertz reflection images", *Journal of Infrared, Millimeter, and Terahertz Waves*, (2018).

- E. Castro-Camus, J. Ornik, C. Mach, G. G. Hernandez-Cardoso, B. Savalia, J. Taiber, A. Ruiz-Marquez, K. Kesper, S. Konde, C. Sommer, J. Wiener, D. Geisel, F. Hüppe, G. Kräling, P. Mross, J. Nguyen, T. Wiesmann, B. Beutel, and M. Koch, "Simple Ventilators for Emergency Use Based on Bag-Valve Pressing Systems: Lessons Learned and Future Steps", *Applied Sciences*, (2020).

- J. M. Seifert, G. G. Hernandez-Cardoso, M. Koch, and E. Castro-Camus, "Terahertz beam steering using active diffraction grating fabricated by 3D printing", *Optics Express*, (2020).

- F. E. M. Lambert, E. S. Reyes-Reyes, G. G. Hernandez-Cardoso, A. Gomez-Sepulveda, and E. Castro-Camus, "In situ determination of the state of conservation of paint coatings on the kiosk of Guadalajara using terahertz time-domain spectroscopy", *Journal of Infrared, Millimeter, and Terahertz Waves*, (2020).

Conference works and presentations

- G. G. Hernandez-Cardoso*, *Early diagnosis of diabetic foot syndrome by terahertz imaging*, 11th THz young scientists meeting, Marburg, Germany, March 1-2 2020.

- G. G. Hernandez-Cardoso*, A. K. Singh, and E. Castro-Camus, *Comparison between effective medium theory models for the dielectric response of biological tissues to terahertz radiation*, (accepted at 9th International THz-Bio Workshop, Erice, Silicy, Italy, April 30 - May 3 2020).

- G. G. Hernandez-Cardoso*, M. Alfaro-Gomez, S. C. Rojas-Landeros, I. Salas-Gutierrez, and E. Castro-Camus, *Early screening of diabetic foot syndrome by terahertz imaging*, (accepted at 9th International THz-Bio Workshop, Erice, Silicy, Italy, April 30 - May 3 2020).

- G. G. Hernandez-Cardoso*, A. K. Singh, E. Castro-Camus, *Comparison between effective medium theory models for biological tissues in the THz range* , 44rd International Conference on Infrared, Millimeter, and Terahertz Waves (IRMMW-THz), Paris, France, September 1-6 2019.

- A. K. Singh, A. V. Perez-Lopez, J. Simpson, G. G. Hernandez-Cardoso*, and E. Castro-Camus, *Three-dimensional water mapping of succulent Agave victoriae reginae leaves by terahertz imaging*, 44rd International Conference on Infrared, Millimeter, and Terahertz Waves (IRMMW-THz), Paris, France, September 1-6 2019.

- D. I. Ramos-Soto, A. K. Singh, E. Saucedo-Casas, E. Castro-Camus, G. G. Hernandez-Cardoso*, and M. Alfaro-Gomez, *Visualization of moisturizer effects in stratum corneum in vitro using THz spectroscopic imaging*, 44rd International Conference on Infrared, Millimeter, and Terahertz Waves (IRMMW-THz), Paris, France, September 1-6 2019.

- G. G. Hernandez-Cardoso, M. Alfaro-Gomez, S. C. Rojas-Landeros, I. Salas-Gutierrez, and E. Castro-Camus*, *Three-color spectroscopic terahertz images as an indicator for diabetic foot syndrome deterioration*, 43rd International Conference on Infrared, Millimeter, and Terahertz Waves (IRMMW-THz), Nagoya, Japan, September 9-14 2018.

- G. G. Hernandez-Cardoso*, M. Alfaro-Gomez, S. C. Rojas-Landeros, I. Salas-Gutierrez, and E. Castro-Camus, *Diabetic foot early diagnosis and statistical analysis by spectral terahertz reflection images*, SPIE Optics + Photonics, San Diego, California, USA, August 9-14 2018.

- G. G. Hernandez-Cardoso*, *Diagnóstico temprano de pie diabético por imágenes espectroscópicas de terahertz*, Coordinación para la Innovación y Aplicación de la Ciencia y la Tecnología (CIACyT), San Luis Potosí, SLP, México, June 1st 2018 (Invited seminar).

- G. G. Hernandez-Cardoso*, S. C. Rojas-Landeros, M. Alfaro-Gomez, A. I. Hernandez-Serrano, I. Salas-Gutierrez, E. Lemus-Bedolla, A. R. Castillo-Guzman, H. L. Lopez-Lemus, and E. Castro-Camus, *Early screening of diabetic foot by terahertz imaging*, Taller de Nanolitografía y Conferencia NanoTerahertz, San Luis Potosí, SLP, México, November 8-10 2017.

- G. G. Hernandez-Cardoso, S. C. Rojas-Landeros, M. Alfaro-Gomez, A. I. Hernandez-Serrano, I. Salas-Gutierrez, E. Lemus-Bedolla, A. R. Castillo-Guzman, H. L. Lopez-Lemus, and E. Castro-Camus*, *Development of evaluation of diabetic foot deterioration by terahertz sprectroscopic image*, 42rd International Conference on Infrared, Millimeter, and Terahertz Waves (IRMMW-THz), Cancún, Quintana Roo, México, August 27 - September 1st 2017.

Acknowledgements

First of all I would like to thank the support of Consejo Nacional de Ciencia y Tecnología (México) for the scholarship allowing me to perform the research presented in this thesis.

I am deeply grateful to my supervisor Dr. Enrique Castro Camus for his invaluable support, guidance and advise during my doctoral process. I also want to thank my colleagues from the Applied Terahertz Science Group for the nice time we spent in and outside the lab. To Dr. Abhishek K. Singh for the support on the effective medium theory models comparison. To Gerardo Gutierrez and Edgar Reyes for their help on the images acquisition of the MMAT clinical study. To Dra. Blanca Murillo for giving us the opportunity to perform the clinical study at the Unidad Médica de Alta Especialidad del Instituto Mexicano del Seguro Social T1 in León, Guanajuato. To Dr. Fabián Amador for his help in the recruitment of diabetic and non-diabetic subjects, and the compilation of clinical data and golden standard test results. To Carolina Rojas and Dra. Mariana Alfaro for their support in the proof-of-concept study that led to the RYG-color-coded images analysis. To Dr. Irving Salas for his guidance and discussion of the medical aspects of this research. Thank you all!

Although mostly of the work presented in this report was developed in México, the data analysis of the clinical study and this thesis writing were performed during my research stay in Marburg, Germany. I could not thank enough my host Prof. Dr. Martin Koch and all the Semiconductor Photonics group members for the warm welcoming, specially Caro Sommer, Franzi Hüppe, Christian Birk and Johnny Nguyen, this process far away from home would have not been possible without your great support and friendship. Vielen Dank, ihr seid die Allerbesten!

Pero sobre todas las cosas quiero agradecer a mi familia. A mis papás Lupita y César por su entrega, amor y apoyo incondicional. A mis hermanos Pablo, Marycarmen y Alejandra por ser mis mejores amigos y cómplices de vida. Nada de esto habría sido posible sin ustedes. Los quiero mucho. ¡Muchas gracias por todo!

Thesis contribution declaration

The studies presented in this report were conceived and performed during my PhD process. Nevertheless, it is important to mention that the Moisture Mapping by Teraherz (MMAT) proof-of-concept study was developed as part of my Masters Degree, including the MMAT v1 scanner and the data acquisition which were used in this work for the further implementation of the RYG-images.

Contents

Chapter 1

Introduction

Advances in medical imaging as diagnostic technique have helped in the prevention and treatment of many health conditions during the history of mankind, prolonging the life expectancy of human beings. Timely diagnosing a disease increases the probabilities to overcome it, helping in the proper treatment for preventing its consequences. With the first X-ray image in 1895, diagnostic radiology was born as a medical speciality which uses imaging to diagnose or treat diseases [1], paving the road for the introduction and improvement of imaging techniques for the visualization of the human body.

Light and most of the radiation within the electromagnetic spectrum have played an important role on medical imaging techniques for the diagnosis and treatment of multiple diseases. For instance, radiography, which comprises the broad area of x-rays, is used not only to visualize bones and organs inside the human body as diagnostic technique but it is also used for the treatment of many diseases and types of cancer. Other imaging techniques, as magnetic resonance imaging, use magnetic fields and radio frequencies to visualize soft tissue contrast. Although non-ionizing, this technique has the disadvantage that the patient has to hold still for long periods of time in a noisy, cramped space while the imaging is performed. High-frequencies sound waves, known as ultrasound, are also

used to visualize soft tissue structures in the body. However, the quality of the images obtained is compromised by the skills of the person performing the test. Other approaches, as nuclear medicine, involve the administration of radioactive tracers to the patient, and the radiation emitted, e.g. gamma rays, by the tracer in the body is displayed as an image [1].

Yet and despite all the existing imaging techniques, there are many important health conditions affecting people in the world which are not properly diagnosed and treated due to the lack of an objective and quantitative diagnostic test, such is the case of diabetic foot syndrome. This condition causes ulceration in the lower limbs of about 15% [2] diabetic patients which leads to amputation in about 2.5% of diabetics [3]. Early stages of diabetic foot syndrome are either subjectively or indirectly diagnosed.

The number of application of terahertz radiation in the biological and medical fields has exploded in recent years, owing to its unprecedented sensitivity to the water content of tissues [4]. In addition, this technique is non-invasive and entirely harmless to living organisms, given that terahertz photons have around three orders of magnitude less energy than that needed for ionization, and that most terahertz time-domain spectroscopy sources operate in the sub-$1\,\mu$W power regime [5]. Terahertz has been used to detect skin [6], breast [7], colon [8, 9], and other types of cancer [10], as well as a tool to determine the severity of skin burns [11, 12], which is not always easy to diagnose clinically. In this thesis, terahertz reflection imaging is proposed as a non-invasive and non-ionizing technique for the objective and quantitative evaluation of deterioration in the feet of diabetic patients as an early diagnosis of diabetic foot syndrome.

1.1 The terahertz band

The terahertz (THz) band refers to the interval of radiation with frequencies between 300 GHz and 10 THz (1 mm to 30 μm, or 1 meV to 41 meV). Located in the electromagnetic spectrum in between microwave and infrared radiation, as illustrated in Figure 1.1, this frequency breach, enclosed by the electronics and optics limits, was inaccessible due to the lack of devices capable of emitting and detecting terahertz radiation [13]. From the microwaves side, electric circuits are not capable of oscillating at frequencies high enough to produce terahertz radiation [14]. From the other side, given that the photon energy of terahertz radiation is comparable to the thermal energy at room temperature, conventional photo-detectors either have to be kept at cryogenic temperatures or have a relatively poor noise performance for the detection of terahertz waves [15].
It was until the 1980s, with the invention of the ultrashort pulsed laser, that the terahertz band was reachable and the radiation generation and detection was achieved using photoconductive antennas (PCA) [16, 17]. Later developments, as terahertz sources and detectors based on optical rectification, led to the introduction of the Terahertz Time-Domain Spectroscopy (THz-TDS) technique [18–20]. This technique records the temporal waveform of the terahertz electric field and, by converting the data to the frequency domain, the amplitude and spectral phase information of the waveforms are obtained simultaneously. This allows direct measurements of optical properties of the probed materials.
Terahertz radiation has particular characteristics that allow a wide variety of applications [21]. Terahertz waves can propagate through a number of dielectric materials - paper, wood, cardboard, plastics, ceramics, clothing - but do not penetrate liquid water nor metals [13]. Terahertz radiation is non-ionizing and entirely harmless to living organisms, so it is of interest in biomedical applications [22, 23].

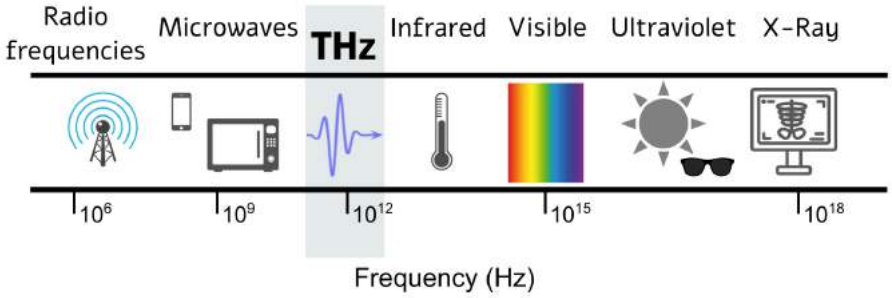

Figure 1.1: The electromagnetic spectrum. The terahertz band is located in between microwaves and infrared radiation. Bands of the spectrum are indicated from radio frequencies to x-rays as a function of their frequency. Common sources of radiation are shown for the different regions of the spectrum.

1.1.1 Terahertz applications

Due to the properties of terahertz radiation, terahertz waves have increasingly been used to the study of materials and physical processes over the last few years. The number of applications of the terahertz time-domain spectroscopy technique is still growing in many different fields like security, telecommunications, cultural heritage, biomedical imaging, industry applications and, physical processes, as molecular dynamics and intraband transitions in semiconductor materials. A brief description of some of these applications is listed below.

- **Molecular dynamics.** Compared to radio waves and infrared radiation, terahertz are very sensitive to some molecule dynamics, particularly to water collective motions. Some other spectral signatures of organic and biological molecules in the THz region are associated with large amplitude vibrational motions and inter-molecular interactions. THz spectroscopy is capable of analyzing these molecular dynamics and has been applied to the study of the hydration dynamics of aqueous solutions and to the quantification of substances as glucose, alcohols and oils [24–29].

- **Semiconductor materials.** Time resolved studies have been performed using terahertz time-domain spectroscopy in order to understand the carrier dynamics in semiconductor materials. This technique has allowed

studying quasiparticle formation in photoexcited carriers and monitoring the temporal evolution of their conductivity with sub-picosecond time resolution [30–32].

- **Security imaging.** Terahertz radiation penetrates into dielectric materials but metals are highly reflective at terahertz frequencies, furthermore, several substances, such as aspirin and methamphetamine, have special fingerprints in the THz frequency region [33, 34]. Therefore, terahertz radiation has been used for the inspection of sealed packages and the detection of weapons, drugs and explosives [35, 36].

- **Communications.** The THz frequency band offers a great communications bandwidth. Although THz waves are strongly absorbed by water vapor limiting their propagation through the atmosphere, data transmission in this frequency range has been achieved [37]. THz sources, modulators, components and devices are being explored for indoor high-speed wireless communications [38–43].

- **Cultural heritage.** Wood, ceramics, fabrics and many pigments are transparent to terahertz radiation. Terahertz time-domain spectroscopy is a non-destructive technique to analyze the internal structure of different artwork pieces. Terahertz waves have been used to retrieve thickness and depth of painting layers for conservation and restoration purposes [44, 45].

- **Biomedical imaging.** Since THz radiation is non-ionizing it does not cause biological damage and can be safely used in living tissue [46]. Water is highly absorptive in the THz region and a fundamental part in biological systems, hence, conditions related to hydration changes can be studied with terahertz waves. THz-TDS has been used to monitor hydration and dehydration dynamics of biological samples [47, 48] and to characterize living tissue for tumor detection [6, 10, 49], burns evaluation [11, 12] and dental cavities diagnosis [50, 51].

1.2 Objectives

The objective of this work is the exploration of medical applications of terahertz radiation for the diagnosis and evolution of diseases. Particularly, proposing terahertz imaging as an early diagnosis technique of diabetic foot syndrome. Furthermore, given that terahertz biomedical applications are often based on the effective medium theory for the quantification of water content in living tissue, it is of interest performing a comparative study on effective medium theory models.

In Chapter 2 an introduction to the fundamentals of terahertz time-domain spectroscopy is provided for the understanding of the diagnosis technique basis. A typical terahertz time-domain spectrometer is presented, followed by the description of terahertz emission and detection by photoconductive antennas. The terahertz time-domain spectroscopy technique is described for transmission and reflection geometries together with a description of the terahertz time-domain imaging technique, all three terahertz time-domain spectroscopy approaches used to perform the studies presented in this work. Details on the THz systems employed in this thesis are also provided. The interaction between terahertz waves and biological tissue is reviewed by the end of the Chapter.

In Chapter 3 an empirical comparison between effective medium theory models for the dielectric response of biological tissue at terahertz frequencies is developed in order to determine the most suitable theory for modeling biological tissues in the terahertz range. An introduction to the effective medium theory is given together with the description of the three most employed effective medium models in the terahertz regime. The terahertz spectroscopic measurements performed on water-basil binary mixtures and the analysis of their dielectric function with the effective medium theory models are presented. The biological relevance of the models in the context of our experimental data based on their fundamental assumptions is further discussed.

In Chapter 4, the Moisture MApping by Terahertz (MMAT) technique is proposed for the evaluation of the diabetic foot deterioration as an early diagnosis

test and ulcer prevention tool. An introduction on diabetes mellitus, diabetic foot syndrome and the existing diagnosis tests is provided followed by a brief description of a proof-of-concept study using terahertz imaging as a potential diagnostic technique for the diabetic foot syndrome. The MMAT scanner, the data acquisition and the imaging processing for the water content retrieval are described.

In Chapter 5 RYG-color-coded images are proposed for the easy identification of foot sole areas in risk of ulceration. The data processing for the RYG-images construction is described and a pixel statistical analysis is provided.

Finally, a clinical trial of the MMAT technique is presented in Chapter 6 to explore the potential of the proposed diagnostic test. A normality study between diabetic and non-diabetic subjects is provided together with a study for the classification of diabetic patients according to the complications related to the diabetic foot syndrome. The statistical analysis for the proposed technique as a diagnostic test is performed. To conclude this thesis, in Chapter 7 the results and conclusions of the studies presented are summarized.

Chapter 2

Terahertz time-domain spectroscopy (THz-TDS)

The possibility of generating and detecting terahertz radiation, together with improvements in ultrashort pulsed lasers, and advances in semiconductor materials and electro-optic cyrstal growth, led to the development of the terahertz time-domain spectroscopy (THz-TDS) technique [19, 52–58]. Whilst most spectroscopic techniques are based on recording the intensity of radiation transmitted through a sample as a function of the frequency or wavelength, THz-TDS records the electric field transmitted through the sample. This converts THz-TDS into a phase sensitive technique, allowing the direct measurement of the complex dielectric properties of materials [59, 60].

2.1 THz-TDS system

Spectroscopic studies with the THz-TDS technique are performed using a time-domain spectrometer. The THz-TDS spectrometer consists of an ultrashort pulsed laser, a delay line, a terahertz emitter, a terahertz detector, and a set of optical components to drive the radiation along the system. A schematic diagram of a time-domain spectrometer is shown in Figure 2.1.

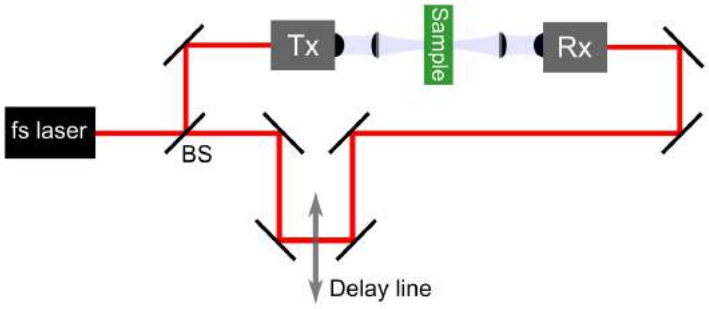

Figure 2.1: Diagram of a terahertz time-domain spectrometer in transmission geometry. The ultrashort pulse is divided by a beam splitter. One part is guided by a mirror to the transmitter for the terahertz generation, the other part is guided by a set of mirrors through the delay line and subsequently to the receiver for the terahertz detection.

The near-infrared laser provides ultrashort pulses, each cycle of radiation is divided into two optical pulses by a beam splitter. One of the pulses is driven to the THz emitter, the generated THz radiation is collected, collimated, and then focused onto a sample by a pair of lenses. A second pair of lenses are used to collect the radiation after interacting with the sample and to refocus it onto the detector. The beam path of the second optical pulse is varied by a delay line for the detection of the THz radiation coming from the sample. The emission and detection processes are further described in the next paragraph.

2.1.1 Emission and detection of terahertz radiation

The emission and detection of terahertz radiation can be performed by many different methods as photoconductive antennas (PCA) for photomixing, and electrooptic (EO) crystals for optical rectification and phase matching [13,16,18]. The terahertz systems used for the development of the studies presented in this thesis use photoconductive antennas for the emission and detection of terahertz radiation.

Terahertz generation by PCA

A photoconductive emitter consists of a pair of metallic electrodes on top of a semiconductor substrate [17,61]. An external biasing voltage is applied between the electrodes. For the terahertz emission, an ultrashort laser pulse incides on the gap between the electrodes, generating photocarriers. These electron-hole pairs are accelerated by the external electric field giving rise to an electromagnetic transient that will be radiated with frequency components around 1.0 THz [62]. The emission process is graphically represented in Figure 2.2.

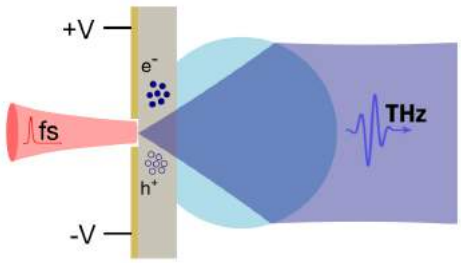

Figure 2.2: Terahertz generation by a photoconductive antenna. The optical pulse incides on the semiconductor substrate creating electron-hole pairs, the voltage applied to the antenna accelerates the charge carriers emitting terahertz radiation. An hyperemispheric lens is used to collimate the radiation generated.

Terahertz detection by PCA

Analogous to a photoconductive emitter, a photoconductive receiver consists of a pair of metallic electrodes deposited on a semiconducting material. For the terahertz detection, ultrashort laser pulses synchronised with THz transients are focused with constant relative delay on the gap between the electrodes. The laser pulse generates photocarriers which are accelerated from that instant following the action of the THz electric field. This charge acceleration produces a current between the two electrodes. Finally, since the optical pulses are approximately a hundred times shorter than the THz pulse, the photocurrent between the electrodes would be proportional to the integral of the electric field for each value of the relative delay given by [62]

$$J(t) = \int_{-\infty}^{+\infty} E_{\mathrm{THz}}(t')\sigma(t-t')dt', \tag{2.1}$$

where $J(t)$ is the photocurrent, E_{THz} is the THz electric field, t is the relative time delay between pulses and σ is the conductivity of the antenna induced by the ultrashort pulse. A graphical representation of the terahertz detection process can be observed in Figure 2.3.

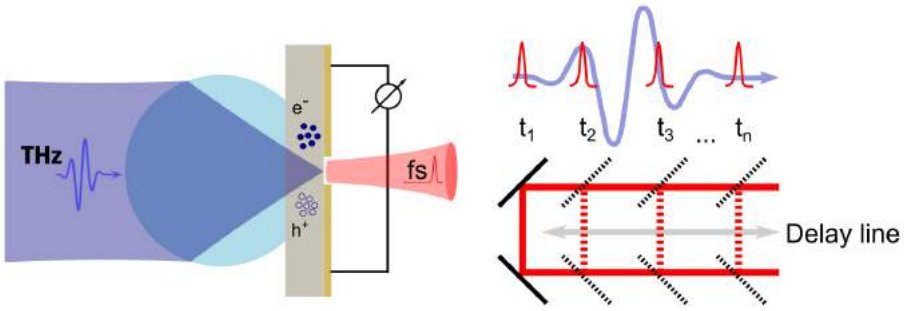

Figure 2.3: Terahertz detection by a photoconductive antenna. Optical pulses, delayed in time, incide on the semiconductor substrate creating electron-hole pairs, the charge carriers are accelerated by the terahertz pulse generating a measurable photocurrent. An hyperemispheric lens is used to focus the terahertz radiation onto the substrate.

2.2 THz-TDS technique

In order to perform spectroscopic studies with the THz-TDS technique, an electric field is recorded as function of time using a time-domain system. Subsequently, the recorded data is processed to retrieve the optical properties of the material under study. Terahertz time-domain systems can be configured in either transmission or reflection geometry as shown in Figure 2.4.

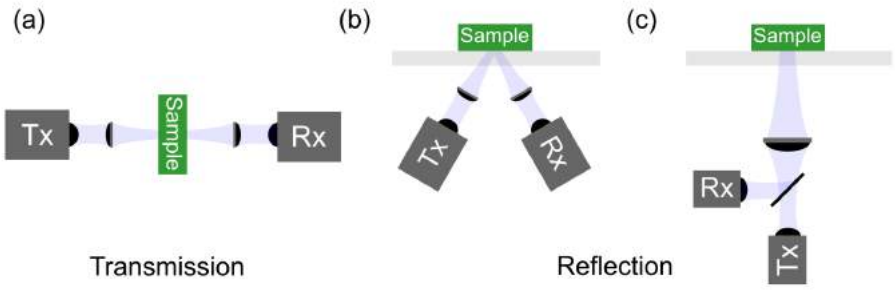

Figure 2.4: Terahertz time-domain system in transmission (a) and reflection geometry, (b) and (c) . Terahertz radiation is collected from the transmitter (Tx) and focused onto the sample. The radiation transmitted or reflected is collected from the sample and focused onto the receiver (Rx).

In transmission geometry, the transmitter and receiver are facing each other with four lenses forming a single optical axis that collects the terahertz radiation from the transmitter, focuses it onto the sample, collects the transmission and focuses it again onto the receiver, Fig. 2.4 (a). In reflection geometry, the transmitter and receiver can either be placed facing two optical axes a certain angle from each other, Fig.2.4 (b) or orthogonally aligned with a beam splitter and a lens to form a normal incidence system Fig.2.4 (c). The optical components collect and focus the terahertz radiation from the transmitter onto the sample and then, collect and focus the reflected radiation onto the receiver.

The analysis of the recorded electric field depends on the THz radiation propagation throughout the emitter-sample-detector optical path. In the following, the THz-TDS technique to extract the optical properties of materials is described for transmission and reflection geometries.

Transmission

The optical properties of a material can be investigated by studying the terahertz radiation transmitted through the sample. At first, a reference electric field $E_{\mathrm{ref}}(t)$ is recorded in the absence of sample. Subsequently, the sample is located in the optical path and an electric field $E_{\mathrm{sam}}(t)$ is recorded too. The reference and sample electric fields would be shifted in time with respect to each other as a result of the delay caused by the refractive index of the sample. Furthermore, the electric field transmitted through the sample $E_{\mathrm{sam}}(t)$ would be smaller in size and different in shape. The difference in size is caused by the Fresnel reflection at the faces of the sample and by the absorption throughout the sample. The shape difference could be attributed to dispersion and non-uniform absorption as a function of frequency.

Both electric fields $E_{\mathrm{ref}}(t)$ and $E_{\mathrm{sam}}(t)$ are Fourier transformed in order to obtain the spectral amplitude and phase as function of frequency. Let $\tilde{E}_{\mathrm{ref}}(\omega) = \mathcal{E}_{\mathrm{ref}}(\omega)e^{i\phi_{\mathrm{ref}}(\omega)}$ and $\tilde{E}_{\mathrm{sam}}(\omega) = \mathcal{E}_{\mathrm{ref}}(\omega)e^{i\phi_{\mathrm{sam}}(\omega)}$ denote the corresponding Fourier transforms. The complex transmission through the sample $\tilde{T}$ is given by

$$\tilde{T}(\omega) = \frac{\tilde{E}_{\mathrm{sam}}(\omega)}{\tilde{E}_{\mathrm{ref}}(\omega)} = \frac{\mathcal{E}_{\mathrm{sam}}(\omega)}{\mathcal{E}_{\mathrm{ref}}(\omega)} e^{i(\phi_{\mathrm{sam}}(\omega) - \phi_{\mathrm{ref}}(\omega))}. \tag{2.2}$$

The transmission can also be written in terms of the complex refractive index of the sample $\tilde{n} = n + i\kappa$, and the Fresnel transmission $t_{12} = 2/(\tilde{n}+1)$ and $t_{21} = 2\tilde{n}/(\tilde{n}+1)$ at the surfaces of the sample as

$$\tilde{T}(\omega) = t_{12}(\omega)t_{21}(\omega)e^{i\frac{\omega d}{c}(\tilde{n}(\omega)-1)}FP(\omega), \tag{2.3}$$

where d is the thickness of the sample, and $FP(\omega)$ is the Fabry-Perot term that includes multiple internal reflections of the THz pulse in the sample given by

$$FP(\omega) = \sum_{k=0}^{\infty} \left[-\frac{(\tilde{n}(\omega)-1)^2}{(\tilde{n}(\omega)+1)^2} e^{i(2\tilde{n}(\omega)\omega d)/c} \right]^k. \tag{2.4}$$

For thick samples, compared to the wavelength, it is possible to avoid the presence of internal reflections in the time domain electric field data, hence $FP(\omega)$ is neglected and by combining Eq. 2.2 and Eq. 2.3 the refractive index can be extracted analytically as

$$n(\omega) = 1 + \frac{c(\phi_{\text{sam}}(\omega) - \phi_{\text{ref}}(\omega))}{\omega d}, \tag{2.5}$$

$$\kappa(\omega) = -\frac{c}{2\omega d} \ln \left[\frac{1}{t_{12}(\omega) t_{21}(\omega)} \frac{\mathcal{E}_{\text{sam}}(\omega)}{\mathcal{E}_{\text{ref}}(\omega)} \right], \tag{2.6}$$

In case of thin samples the refractive index can be extracted by solving Eq. 2.3 numerically [59, 63, 64].

The process of the THz-TDS technique, from recording the terahertz signal to extracting the complex refractive index of the material, is graphically represented in Figure 2.5. The transmitted electric field is recorded, Fourier transformed to obtain the spectral information to finally extract the complex refractive index of the sample.

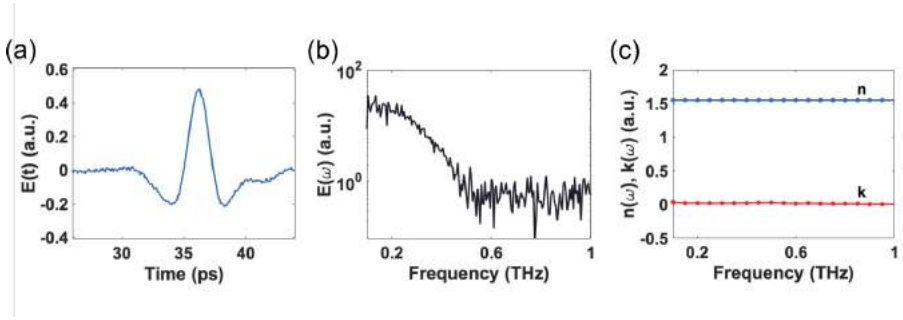

Figure 2.5: Graphic representation of the method for extracting the complex refractive index, $\tilde{n} = n + i\kappa$. (a) The electric field is recorded, (b) Fourier transformed to obtain the spectral amplitude and phase to finally determine the (c) refractive index, n, and extinction coefficient of the sample, κ.

Reflection

The THz-TDS technique in reflection geometry is useful when the materials to be investigated are highly absorptive or the samples are thick enough for terahertz transmission. In reflection configuration, the reference electric field $E_{\mathrm{ref}}(t)$ can be recorded by placing a reflector, for instance a metal mirror, in the measurement plane. Subsequently, the metal mirror is replaced by the sample and an electric field $E_{\mathrm{sam}}(t)$ is recorded again. The electric fields $E_{\mathrm{ref}}(t)$ and $E_{\mathrm{sam}}(t)$ are Fourier transformed in order to obtain the spectral amplitude and phase as function of frequency. Being $\tilde{E}_{\mathrm{ref}}(\omega)$ and $\tilde{E}_{\mathrm{sam}}(\omega)$ the corresponding Fourier transforms, the complex reflectivity of the sample $\tilde{R}$ is given by

$$\tilde{R}(\omega) = \frac{\tilde{E}_{\mathrm{sam}}(\omega)}{\tilde{E}_{\mathrm{ref}}(\omega)}. \tag{2.7}$$

The reflectivity can also be written in terms of the Fresnel reflection $\mathrm{r_{sam}}$ at the surface of the sample as

$$\tilde{R}(\omega) = \frac{\tilde{E}_{\mathrm{in}}(\omega)\mathrm{r_{sam}}}{\tilde{E}_{\mathrm{in}}(\omega)} = \mathrm{r_{sam}}, \tag{2.8}$$

where $\tilde{E}_{\mathrm{in}}$ is the incident electric field, and $\mathrm{r_{sam}}$ is given by the complex refractive index of the sample $\tilde{\mathrm{n}}_{\mathrm{sam}} = \mathrm{n} + \mathrm{i}\kappa$ and the angle of incidence ϕ as

$$\mathrm{r_{sam}} = \frac{\sqrt{1-\sin^2\phi} - \sqrt{\tilde{\mathrm{n}}^2_{\mathrm{sam}} - \sin^2\phi}}{\sqrt{1-\sin^2\phi} + \sqrt{\tilde{\mathrm{n}}^2_{\mathrm{sam}} - \sin^2\phi}}, \tag{2.9}$$

The complex refractive index of the material can then be extracted by using Eq. 2.7 and numerically solving Eqs. 2.8 and 2.9.

It is important to notice that this approach is very sensitive to the precise placement of the reference with respect to the sample surface. Any slight displacement between the reference and sample measurement planes might lead into errors in the calculation of the materials' optical parameters. Additionally, some compensation in the analysis is required [65].

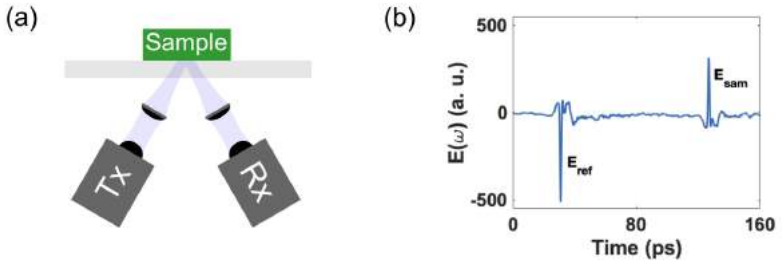

Figure 2.6: THz-TDS in self-reference reflection geometry. (a) The sample is placed in contact with a thick window. (b) The recorded signal consists of two pulses, the first one reflected at the air-window interface, the second from the window-sample reflection. The separation in time between the pulses is proportional to the thickness of the measurement window.

A different approach to eliminate the need to replace the sample with a metal mirror is placing the sample in contact with a thick transparent measurement window, such as silicon, quartz or high-density polyethylene (HDPE) [66]. In this method, known as self-reference reflection THz time-domain spectroscopy, the reflected waveform as a function of time consists of both the reference and the sample pulses separated in time. The reference pulse is given by the reflection at the air-window interface and the sample pulse results as the reflection in the window-sample interface. The geometry of this method and the corresponding recorded signal is shown in Figure 2.6.

The optical properties of the sample can be described by studying the terahertz radiation reflected by the sample. The complex reflectivity of the sample $\tilde{R}$ is given by

$$\tilde{R}(\omega) = \frac{\tilde{E}_{\mathrm{sam}}(\omega)}{\tilde{E}_{\mathrm{ref}}(\omega)}. \tag{2.10}$$

The reflectivity can also be described in terms of the Fresnel transmission and reflection at the interfaces. As illustrated in Figure 2.7, an incoming terahertz pulse $\mathrm{E_{in}}$ incides onto the measurement window, a part of the pulse is reflected at the first surface and is given by

$$\mathrm{E_{ref}} = \mathrm{E_{in}} \mathrm{r}_{12}. \tag{2.11}$$

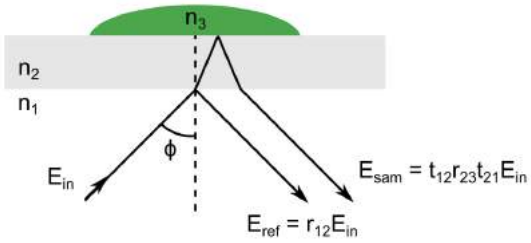

Figure 2.7: Ray schematic of the terahertz radiation path in THz-TDS self-referenced reflection geometry. The input THz signal splits into a reference and a sample signal. The output signals are described by the input THz signal, and the transmission and reflection at the interfaces.

The transmitted part propagates through the window and reaches the window-sample interface, in which the pulse is partly reflected; that reflection propagates again through the window, and part of it is transmitted at the interface and given by

$$\mathrm{E_{sam}} = \mathrm{E_{in}} \mathrm{t_{12}} \mathrm{r_{23}} \mathrm{t_{21}} \exp(2i \mathrm{n_2} \omega d/c). \tag{2.12}$$

The electric pulses $\mathrm{E_{ref}}$ and $\mathrm{E_{sam}}$ are Fourier transformed in order to obtain the spectral amplitude and phase as function of frequency and the complex reflectivity of the sample is given by

$$\tilde{\mathrm{R}}_{\mathrm{sam}}(\omega) = \frac{\tilde{\mathrm{E}}_{\mathrm{sam}}(\omega)}{\tilde{\mathrm{E}}_{\mathrm{ref}}(\omega)} = \frac{\mathrm{t_{12}} \mathrm{r_{23}} \mathrm{t_{21}}}{\mathrm{r_{12}}} \exp(2i \mathrm{n_2} \omega d/c), \tag{2.13}$$

where t_{ij} and r_{ij} are the Fresnel transmission and reflection coefficients at the interface between i-th and j-th material, and d is the thickness of the measurement window.

From the beam propagation we can see that in this self-reference approach, the sample pulse is slightly displaced with respect to the reference pulse. To compensate this misalignment, an empirical calibration factor is considered in the modeled reflectivity [26]. Introducing this frequency-dependent calibration

factor, $A_{\mathrm{cal}}(\omega)\Delta_{\mathrm{cal}}(\omega)$, to the sample signal, the complex reflectivity would be

$$\tilde{\mathrm{R}}_{\mathrm{sam}}(\omega) = \frac{\tilde{\mathrm{E}}_{\mathrm{sam}}(\omega)}{\tilde{\mathrm{E}}_{\mathrm{ref}}(\omega)} = \frac{\mathrm{t}_{12}\mathrm{r}_{23,\mathrm{sam}}\mathrm{t}_{21}}{\mathrm{r}_{12}} A_{\mathrm{cal}}\exp(i\Delta_{\mathrm{cal}})\exp(2i\mathrm{n}_2\omega d/c), \tag{2.14}$$

where the calibration factor is determined by measuring air in contact with the window on both sides and given by

$$A_{\mathrm{cal}}\exp(i\Delta_{\mathrm{cal}}) = \frac{\tilde{\mathrm{E}}_{\mathrm{air}}(\omega)}{\tilde{\mathrm{E}}_{\mathrm{ref}}(\omega)} \frac{\mathrm{r}_{12}}{\mathrm{t}_{12}\mathrm{r}_{23,\mathrm{air}}\mathrm{t}_{21}} \exp(-2i\mathrm{n}_2\omega d/c). \tag{2.15}$$

Inserting Eq. 2.15 into Eq. 2.14, the expression for the sample's reflectivity would be

$$\tilde{\mathrm{R}}_{\mathrm{sam}}(\omega) = \frac{\mathrm{r}_{23,\mathrm{sam}}}{\mathrm{r}_{23,\mathrm{air}}} \frac{\tilde{\mathrm{E}}_{\mathrm{air}}(\omega)}{\tilde{\mathrm{E}}_{\mathrm{ref}}(\omega)}, \tag{2.16}$$

where the Fresnel reflection coefficients are given by

$$\mathrm{r}_{23,\mathrm{air}} = \frac{\sqrt{\mathrm{n}_2^2 - \sin^2\phi} - \sqrt{1 - \sin^2\phi}}{\sqrt{\mathrm{n}_2^2 - \sin^2\phi} + \sqrt{1 - \sin^2\phi}} \tag{2.17}$$

and

$$\mathrm{r}_{23,\mathrm{sam}} = \frac{\sqrt{\mathrm{n}_2^2 - \sin^2\phi} - \sqrt{\tilde{\mathrm{n}}_3^2 - \sin^2\phi}}{\sqrt{\mathrm{n}_2^2 - \sin^2\phi} + \sqrt{\tilde{\mathrm{n}}_3^2 - \sin^2\phi}}, \tag{2.18}$$

n_2 is the refractive index of the window material and ϕ the angle of incidence, which in practice are known. Inserting these reflection coefficients into Eq. 2.16, results in an expression relating the ratio of the sample and reference signals and the complex refraction index of the sample. Then, the sample complex refractive index can be found by solving Eq. 2.16 with respect to $\tilde{\mathrm{n}}_3$ [64, 67]. Finally, the complex refractive index is related to the dielectric function of the material through the relation $\tilde{\varepsilon} = \varepsilon' + i\varepsilon'' = \tilde{\mathrm{n}}^2 = (\mathrm{n} + i\kappa)^2$

2.3 Terahertz time-domain imaging (THz-TDI)

As part of the terahertz science evolution, new technologies have emerged to further explore this radiation band and its variety of applications. A relatively new technique, based on terahertz time-domain spectroscopy, is terahertz time-domain imaging (THz-TDI) or T-ray imaging. THz-TDI is an imaging technique that maps the interaction between terahertz waves and matter [68–71].

Taking advantage of using both amplitude and phase information contained in THz waveforms, a plethora of applications have been already investigated with THz-TDI. Since THz radiation penetrates deep into dielectric and nonmetallic materials, T-ray imaging devices have been used in security imaging for the nondestructive inspection of sealed packages [36] and, because of the spectral fingerprints that several substances have in the THz frequency region, for the detection and identification of weapons, explosives, and chemical and biological agents hidden underneath covering materials [34, 35]. Tomographic T-ray imaging, in which waveforms reflected from an object can be used to form a three-dimensional representation, has also been explored for moisture mapping in leaves [68, 72], archaeological and ancient artifacts investigations [73], materials, buildings, and architectural art inspections [74–77], and for food [78–80] and pharmaceutical [81–83] industry applications. Cultural heritage has also been broadly studied using THz-TDI. THz images have been performed on art paintings [45, 84–87], medieval manuscripts [88], mummies [89, 90] and even on immovable cultural heritage objects [91] for the investigation of paint layers and coatings, sub-surface air gaps, delaminations, and the detection and quantification of pigments.

One of the most promising areas for terahertz imaging technologies is the medical field. The big advantage of THz applications in medicine is that terahertz radiation is non-ionizing and T-ray imaging devices are contactless and non-invasive. Therefore, a medical imaging device based on THz radiation is entirely harmless to the human body. Because water is highly absorptive in the THz region, conditions related to the hydration of biological tissue can be

widely investigated by terahertz imaging. THz-TDI has been applied to spotting cancer tissues [6,9,10], characterizing burn injuries [11,12], studying dental tissue [50,51,92] and, visualizing moisturizer and pressure effects on skin [93,94].

A terahertz imaging system is basically composed by a THz-TDS system and a moving platform for raster-scanning of a target at the focal plane. This technique can be configured, depending on the sample to be investigated, either in transmission or reflection geometry, as seen in Figure 2.8.

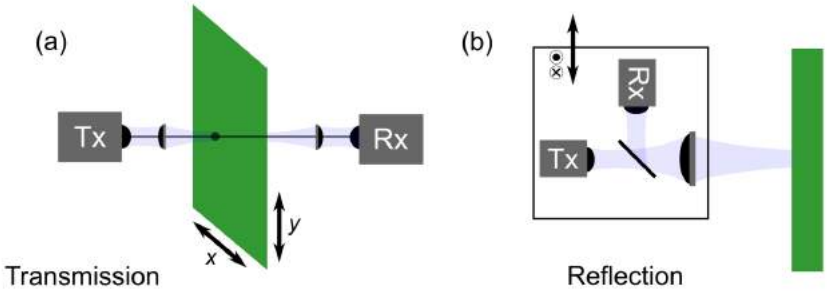

Figure 2.8: Terahertz time-domain imaging in (a) transmission and (b) reflection geometry. Terahertz radiation is collected from the transmitter (Tx) and focused onto the sample. The radiation transmitted or reflected is collected from the sample and focused onto the receiver (Rx). A moving platform is used for raster-scanning the target at the focal plane.

The terahertz imaging technique provides 3D datasets from which spectroscopic information, depth profiles and cross-sectional images of an object can be obtained. Time-domain data provide the possibility of recovering information about the layers, such as thickness, that constitute an object by analyzing the time of flight of the incoming terahertz radiation. In the frequency-domain, T-ray images offer the possibility of identifying materials with particular absorption characteristics in the terahertz band within the imaged objects. THz-TDI data are analyzed depending on the information of interest and the geometry used. In this thesis, a technique based on THz-TDI for the study of the deterioration in the feet skin of diabetic patients is proposed. The technique, set up as well as the data processing are described in Chapter 4.

2.4 Terahertz radiation and biological tissue

The interaction between an electromagnetic wave and a material medium can be described by the optical properties of the material. In order to conduct medical and biological applications with terahertz radiation, it is important to understand the interaction between terahertz waves and biological tissue.

Biological tissue at terahertz frequencies has broadly been studied [4, 95]. Hu *et al.* [68], with the first terahertz image of a fresh leaf, showed that the attenuation of terahertz radiation throughout a biological tissue largely depends on the water within the tissue. Jördens *et al.* [96] presented a model of plant leaves to describe their permittivity at terahertz frequencies. Fitzgerald *et al.* [97] measured the terahertz optical properties of freshly excised human tissue samples of skin, adipose tissue, muscle, artery, vein, and nerve finding significant differences in the refractive index and attenuation coefficient values of the samples. Later, E. Pickwell *et al.* [98] and Gerald J. Wilmink *et al.* [99] measured the complex refractive index of human skin at low terahertz frequencies (0.2 to 1.2 THz). *In vivo* terahertz measurements were performed on the palm, the ventral and dorsal forearm, demonstrating that both the refractive index and the absorption coefficient vary considerably with the water content in the skin. Hernandez-Cardoso *et al.* [100] described the dielectric properties of human skin at terahertz frequencies. Considering human skin as a mixture of water and dehydrated skin, the dielectric properties of dehydrated skin at terahertz frequencies were determined performing terahertz time-domain spectroscopy on dehydrated human skin, and then, the optical properties of human skin for different hydration levels were calculated.

An important factor to take into consideration when studying living beings with electromagnetic waves is the effects of the radiation on biological tissue. The energy of a photon at 1 THz is equal to $6.6\text{x}10^{-22}$ J or 4.1 meV. The necessary energy for ionizing an atom is a thousand times larger. Therefore, THz

radiation is non-ionizing radiation, it does not cause biological damage [22]. Furthermore, given the low energy of THz radiation (0.4 - 40meV), the effects of THz in tissue are limited to thermal effects [23], which due to the powers typically used (1 μm) are completely harmless.

With regard to the optical properties of biological tissue at terahertz frequencies, given that water is a major ingredient in biological tissue and its complex dielectric properties at terahertz frequencies are well known [101], hydrated biological tissue can be seen as the combination of dehydrated tissue and water so the optical properties of the composite system can be described by effective medium theory. The effective medium theory is often used to determine the dielectric function of a medium composed by two or more components, provided that the dielectric function of the components is known, as well as the volumetric fraction they occupy in the medium and, the inclusions in the medium are smaller than the radiation wavelength so the scattering effect can be neglected [102]. Depending on the assumptions about the components of the composite system there are different effective medium theory models. Some models are constructed assuming small, spherical particles embedded in a material with relatively small dielectric function contrast; others allow a great contrast between the dielectric function of the components but are also restricted to spherical inclusions and some more are made for mediums with irregularly shaped particles but require that the components' dielectric functions do not differ much from each other. A further description of the effective medium theory together with an empirical comparison of some models for the dielectric response of biological tissue at terahertz frequencies is provided in the next Chapter.

Chapter 3

Effective Medium Theory

In order to describe and predict the optical properties of a medium consisting of different components (e.g. guest particles embedded in a host), the individual optical properties of the parts involved and their structural geometry should be considered. These host-guest systems can be considered as optically homogeneous effective medium materials, as graphically described in Figure 3.1. The effective medium theory (EMT) takes such an assumption to replace the inhomogeneous composite by a homogeneous material with an effective dielectric function.

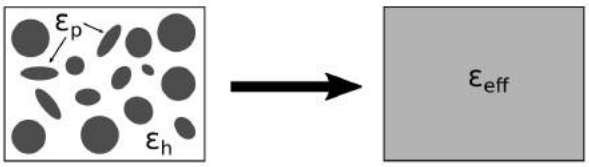

Figure 3.1: Graphic representation of the effective medium theory. A host-guest system can be assumed as an homogeneous medium with effective dielectric properties, $\varepsilon_{\mathrm{eff}}$, given by the combination of the host's (h) and guest particles' (p) dielectric properties, ε_{h} and ε_{p}.

3.1 Effective medium theory (EMT) models

EMT models provide an analytical approach to calculate the macroscopic complex dielectric properties of materials by employing the dielectric properties of their constituents and their volume fractions [102]. The models based on the effective medium theory provide analytical expressions for the optical properties of the complex systems making some assumptions. Since there is a range of effective medium models that, in general differ, a particular one has to be chosen in order to analyze a given system. The frequently used models based on the effective medium theory in order to analyze a composite system at terahertz frequencies are Maxwell-Garnett, Bruggeman, and Landau-Lifshitz-Looyenga [103–105].

Maxwell-Garnett

The Maxwell-Garnett (MG) is a traditional model based on EMT that estimates the aggregate dielectric function of the complex system as

$$\varepsilon_{\text{eff}} = \varepsilon_h \frac{2\mathrm{X}_p\left(\varepsilon_p - \varepsilon_h\right) + \left(\varepsilon_p + 2\varepsilon_h\right)}{\left(2\varepsilon_h + \varepsilon_p\right) + \mathrm{X}_p\left(\varepsilon_h - \varepsilon_p\right)}, \tag{3.1}$$

where ε_h is the dielectric function of the host material, ε_p is that of the guest particles, and X_p is the guest's volume fraction [106]. It is to be noted that this formulation is asymmetric in such a way that if the host and guest materials are exchanged the effective dielectric function ε_{eff} would be different. The asymmetry enhances when the difference in the dielectric functions of the constituents is large [106]. In addition, as the volumetric fraction of the inclusions increases, the assumptions are violated as the effective dielectric function changes. Therefore, this model is only valid for low solute concentrations [105].

Bruggeman

The Bruggeman (BM) model is an improved version of MG model [106], and consists of a two-component homogeneous system for the effective dielectric function ε_{eff} given by

$$\varepsilon_{\text{eff}} = \frac{1}{4}\left(\beta + \sqrt{\beta^2 + 8\varepsilon_h\varepsilon_p}\right), \tag{3.2}$$

where

$$\beta = (3\mathrm{X}_h - 1)\,\varepsilon_h + (3\mathrm{X}_p - 1)\,\varepsilon_p,$$

with X_h, ε_h and X_p, ε_p volumetric fractions and dielectric functions of the individual components, and $\mathrm{X}_h + \mathrm{X}_p = 1$. The BM theory is also based on spherical approximation for the guest (solute) but, in contrast to MG model, it is symmetric [106] and allows a large contrast of the components dielectric function for the complex system [105].

Landau-Lifshitz-Looyenga

The Landau-Lifshitz-Looyenga (LLL) model assumes a medium composed by a host and a guest. The LLL equation is given by [107]

$$\sqrt[3]{\varepsilon_{\text{eff}}} = \mathrm{X}_h\sqrt[3]{\varepsilon_h} + \mathrm{X}_p\sqrt[3]{\varepsilon_p} \tag{3.3}$$

where $\mathrm{X}_{h(p)}$ and $\varepsilon_{h(p)}$ denote the volumetric fraction and the complex dielectric function of the host and guest, respectively, and $\mathrm{X}_h + \mathrm{X}_p = 1$.
Unlike the models described above, this theory allows arbitrarily shaped particles [108] but, it is, in principle, inappropriate to describe the optical properties of a system in which its components have large dielectric contrast [104].

3.2 Empirical comparison between EMT models

In the terahertz regime, particularly in medical and biological applications, EMT has been used for the quantification of water content in biological tissues [46, 47, 96, 100, 109–112]. However, owing to the differences in conditions, it is not clear which of the models is most appropriate, since it must be taken into account that the biological tissue is composed, to a large extent, of water whose dielectric function is much greater than that of any other component of the tissue; in addition, for biological tissues it is hard to define the size or shape of an inclusion, since biological tissues present mesoscopic (pores, vasculature, etc.) and microscopic (cells, membranes, etc.) structure and water is distributed in between this plethora of structural features.

A comparative analysis of the Maxwell-Garnett, Bruggeman and Landau-Lifshitz-Looyenga models, for the determination of water content in biological tissues from terahertz spectroscopic measurements is provided in the following. A mixture of *Ocimum basilicum* (basil) tissue and water was considered as a model system with terahertz dielectric properties similar to a range of soft biological tissues. The dielectric function of dehydrated basil at terahertz frequencies was determined using THz-TDS. Subsequently, binary mixtures of dehydrated and ground basil and water were prepared throughout the host/guest volumetric fraction range (0.0 - 1.0). Terahertz time-domain spectroscopic measurements were performed and the dielectric function of the mixtures was obtained. Moreover, the water content on the mixtures was calculated. A quantitative analysis is provided by calculating the error between experimental and theoretical data.

Determination of dielectric function of dehydrated basil

Basil leaves were dehydrated and ground to powder. The basil powder was used to form five pellets under a pressure of 4 MPa resulting in thicknesses between 1.04 mm and 1.79 mm. With terahertz time-domain spectroscopy, the transmittance of the basil pellet was measured in a nitrogen environment, in order to avoid the water vapor contribution. The data were processed to obtain the dielectric function as described in Chapter 2, Section 2.2. The (a) real and (b) imaginary parts of the complex dielectric function are shown in Figure 3.2.

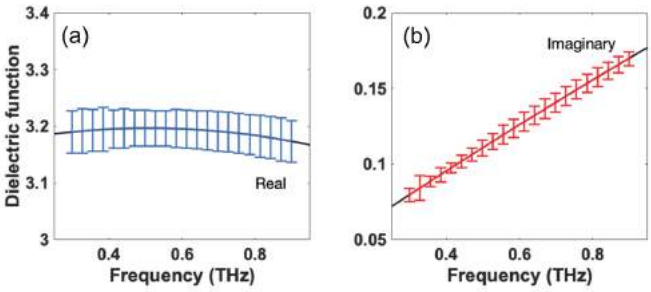

Figure 3.2: Complex dielectric function of dehydrated basil. Dehydrated basil pellets were measured in a nitrogen environment. Second-order polynomials were fitted to the data obtained from five different pellets. The error bars represent the standard deviation of the five measurements. Figure reprinted with permission from [113] © The Optical Society.

Second order polynomials were fitted to both parts of the complex dielectric function. The dielectric function of the dehydrated basil can then be approximated by

$$\varepsilon_R = -0.15\,\mathrm{THz}^{-2} f^2 + 0.16\,\mathrm{THz}^{-1} f + 3.16 \tag{3.4}$$

and

$$\varepsilon_I = -0.01\,\mathrm{THz}^{-2} f^2 + 0.17\,\mathrm{THz}^{-1} f + 0.03 \tag{3.5}$$

where f is the frequency in THz.

Complex dielectric function of water

For terahertz frequencies, the optical properties of water have been broadly studied. The double Debye model describes the interaction between terahertz radiation and water molecules by a complex dielectric function estimated as

$$\varepsilon(\omega) = \varepsilon_\infty + \frac{\varepsilon_0 - \varepsilon_1}{1 + i\omega\tau_1} + \frac{\varepsilon_1 - \varepsilon_\infty}{1 + i\omega\tau_2} \tag{3.6}$$

where τ_1 and τ_2 refer to relaxation times, ε_∞ is the high-frequency permittivity, ε_0 the static permittivity and ε_1 the dielectric constant that describes the transition state between both relaxation processes. These parameters were determined and complemented with two Lorentzian terms by Hans J. Liebe *et al.* [101] as a model of the complex permittivity of water at THz frequencies.

In order to theoretically compare the EMT models, the calculated basil dielectric function, and the water dielectric function given by the double Debye model were used to determine the dielectric function of the water-basil medium for different hydration degrees as shown in Figure 3.3.

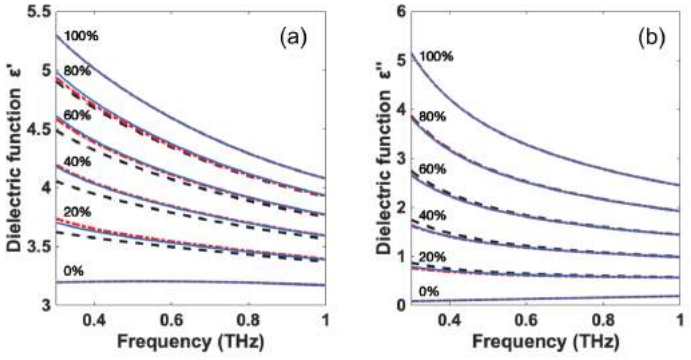

Figure 3.3: (a) Real and (b) imaginary part of the complex dielectric function of water-basil mixture for various hydration degrees given by MG (black dashed lines), BM (red dashed-dotted lines), and LLL (blue solid lines) models in the frequency range from 0.3 THz to 1.0 THz. Figure reprinted with permission from [113] © The Optical Society.

Water-basil mixture preparation

In order to compare the EMT models with experimental data, binary mixtures of water and dehydrated basil powder were prepared by encompassing the entire concentration range. A basil powder was prepared by dehydrating leaves collected from living plants, and grinding them with a mortar and pestle into a fine powder. The hydrated samples were prepared by mixing a known weight of powder with a known volume of water taking into consideration the respective densities. The mass fractions were calculated from volumetric fraction of water by [110]

$$\mathrm{W_w} = \frac{\mathrm{X_w}\rho_\mathrm{w}}{\mathrm{X_w}\rho_\mathrm{w} + \mathrm{X_s}\rho_\mathrm{s}}, \tag{3.7}$$

where

$$\mathrm{X_w} = \mathrm{W_w}\mathrm{M_t} \tag{3.8}$$

and

$$\mathrm{X_s} = (1 - \mathrm{W_w})\mathrm{M_t} \tag{3.9}$$

$\rho_\mathrm{w} = 997\,\mathrm{kg/m^3}$ is the density of water and $\rho_\mathrm{s} = 1099.89\,\mathrm{kg/m^3}$ is the density of the dehydrated basil, W_i denotes the mass fraction, X_i the volumetric fraction, ρ_i the density, M_i the mass of the component and $\mathrm{M_t}$ the total mass of the mixture. The suffixes w and s correspond to water and solid/dry tissue, respectively.

Determination of complex dielectric function of water-dry tissue mixtures

Measurements were made with THz-TDS in order to obtain the mixtures complex dielectric function. A API TeraGauge THz-TDS was used in reflection geometry with normal incidence. The mixtures were placed onto a high density polyethilene (HDPE) window in a kinematic optical mount. A reference electric field $\mathrm{E_{ref}}(t)$ was recorded in the absence of sample. Subsequently the sample was placed and the reflected electric field $\mathrm{E_{sam}}(t)$ was recorded again. In reflection

geometry, the recorded signals are composed of two pulses, the first E_1 comes from the reflection in the air-window interface, while the second E_2 corresponds to the reflection from window-sample interface. Then, the complex refractive index was obtained as described in Chapter 2, Section 2.2. For normal incidence, the expressions to determine the complex refractive index are reduced to

$$\tilde{n}_{sam} = \frac{n_{win}(1 - r_{sam})}{1 + r_{sam}}, \tag{3.10}$$

whit

$$r_{sam} = \frac{R_{sam}}{R_{ref}} r_{air}, \tag{3.11}$$

n_{win} is the refractive index of the HDPE window,

$$r_{air} = \frac{n_{win} - 1}{n_{win} + 1}, \tag{3.12}$$

and $R_{sam(ref)}$ is given by the ratio of $\tilde{E}_{2,sam(ref)}(\omega)$ and $\tilde{E}_{1,sam(ref)}(\omega)$ which are the Fourier transforms of the electric pulses obtained from the sample and reference as explained above. The theoretical dielectric function corresponding to each sample concentration was determined by the MG, BM and LLL models.

Complex dielectric function *vs.* water volumetric fraction

The theoretical dielectric function was obtained as a function of the water volumetric fraction for each of the EMT models under consideration. In the Figure 3.4, these curves are shown as solid black, red and blue lines corresponding to MG, BM and LLL theories, respectively. The grey dots represent the experimental dielectric functions of the mixtures. In this single-frequency comparison at 0.4 THz is possible to see that BM and LLL models approximate the experimental data marginally better for most concentrations, which is consistent with the differences in the dielectric functions resulting from the three models in Fig. 3.3, being BM and LLL closer to each other than MG. Yet, although the experimental dielectric function shown in Fig. 3.4 coincides reasonably well with the theoretical curves, they overlap each other, making it difficult to define

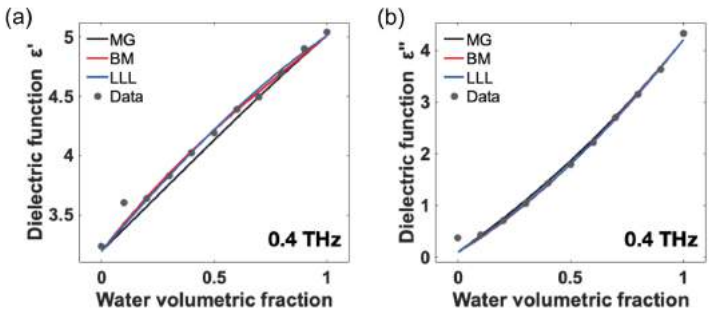

Figure 3.4: (a) Real and (b) imaginary part of the dielectric function of the water-basil mixture as a function of the water volumetric fraction at 0.4 THz. The solid lines in black, red, and blue show the mixture's theoretical dielectric function given by the MG, BM and LLL models, respectively. The grey dots represent the experimental data. Figure reprinted with permission from [113] © The Optical Society.

which of the models fits better the experimental data. Therefore, in order to quantitatively evaluate the three EMT models, the deviation between the experimental and theoretical dielectric function at 0.4 THz was obtained. The real and imaginary dielectric function values are summarized in Table 3.1 and Table 3.2, respectively, together with the corresponding deviations.

Transfer function for reflection measurements and fitting of theoretical models

The quantification of water in the water-basil mixtures was performed via curve fitting to the transfer function, which describes the response of the sample to the terahertz signal. From the response of the sample, the experimental transfer function H_{exp} can be obtained as

$$H_{exp} = \left| \frac{\tilde{E}_{2,sam}}{\tilde{E}_{1,sam}} \right|. \tag{3.13}$$

The corresponding theoretical transfer function can be calculated as

$$H_{theo} = \frac{r_{mix}}{r_{air}} |H_{air}|, \tag{3.14}$$

X_w	Exp.	MG	Δ	BM	Δ	LLL	Δ
0.0	3.24	3.20	0.04	3.20	0.04	3.20	0.04
0.1	3.60	3.38	0.22	3.43	0.17	3.41	0.19
0.2	3.64	3.57	0.07	3.65	0.01	3.62	0.02
0.3	3.83	3.76	0.07	3.85	0.02	3.83	0.00
0.4	4.02	3.94	0.08	4.04	0.02	4.03	0.01
0.5	4.19	4.13	0.06	4.21	0.02	4.22	0.03
0.6	4.39	4.32	0.07	4.38	0.01	4.40	0.01
0.7	4.49	4.50	0.01	4.54	0.05	4.57	0.08
0.8	4.70	4.67	0.03	4.70	0.00	4.73	0.03
0.9	4.90	4.85	0.05	4.85	0.05	4.88	0.02
1.0	5.04	5.01	0.03	5.01	0.03	5.01	0.03
Average			0.07		0.04		0.04

Table 3.1: Real part of the water-basil complex dielectric function resulting from the experimental measurements and the EMT models at 0.4 THz. The corresponding deviations are shown for the mixtures, as well as the average per model.

where r_{air} is given by Eq. 3.12, H_{air} is calculated using Eq. 3.13 in the absence of sample [26], and r_{mix} is the refraction coefficient from the sample given by

$$r_{mix} = \frac{n_{win} - \sqrt{\varepsilon_{mix}(X_w)}}{n_{win} + \sqrt{\varepsilon_{mix}(X_w)}}. \tag{3.15}$$

ε_{mix} is calculated for each of the EMT models for the volumetric fraction X_w that water occupies in the mixture. Least square method was used to fit H_{theo} to H_{exp} in order to obtain the optimal value for X_w.

Theoretical curves of the transfer function for each EMT model were obtained, as well as the experimental transfer function for all the measured mixtures. In Figure 3.5 we can appreciate the experimental data as grey points and the theoretical curves as solid black, red and blue lines for the MG, BM and LLL models, respectively. The data is presented only on the 0.3 THz to 0.4 THz band since this is the part of the spectrum in which our TDS system has the best signal to noise performance.

From the comparison of the three models and the experimental data across the spectral band from 0.3 THz to 0.4 THz presented in Fig. 3.5 it is noticeable that the differences among the three models and, also, the experimental data

X_w	Exp.	MG	Δ	BM	Δ	LLL	Δ
0.0	0.37	0.10	0.27	0.10	0.28	0.10	0.28
0.1	0.43	0.41	0.02	0.37	0.06	0.38	0.04
0.2	0.70	0.75	0.05	0.68	0.02	0.70	0.01
0.3	1.05	1.10	0.05	1.03	0.02	1.04	0.01
0.4	1.43	1.47	0.04	1.40	0.03	1.41	0.02
0.5	1.79	1.87	0.08	1.80	0.02	1.80	0.02
0.6	2.22	2.28	0.06	2.23	0.01	2.23	0.00
0.7	2.71	2.73	0.02	2.69	0.02	2.68	0.03
0.8	3.15	3.19	0.04	3.17	0.02	3.16	0.01
0.9	3.63	3.69	0.06	3.68	0.05	3.67	0.04
1.0	4.34	4.21	0.13	4.21	0.13	4.21	0.13
Average			0.08		0.06		0.05

Table 3.2: Imaginary part of the water-basil complex dielectric function resulting from the experimental measurements and the EMT models at 0.4 THz. The corresponding deviations are shown for the mixtures, as well as the average per model.

are small. The measured transfer function shows some oscillations around the theoretical curves, most likely caused by spurious reflections in the spectroscopy setup that introduce Fabry-Perot spectral oscillations.

Quantification of water in biological tissue: the inverse problem

In order to obtain the hydration degree of a biological medium from the THz measurements, a relationship between the hydration level of tissue and its terahertz optical properties is built as shown in Figure 3.3. Since the biological tissue is considered as the combination of dehydrated tissue and water, and given that the complex dielectric properties of both components are known, the water content in a sample is found by fitting a theoretical function dependent on X_w to the experimental data.

In this study, with the purpose to fully evaluate the three EMT models, a least squares fit algorithm was used to measure the water content in the prepared mixtures. The theoretical transfer function, given by Eq. 3.14, was fitted to its corresponding experimental transfer function. The optimal value for X_w, such that H_{theo} fits H_{exp} best, determines the hydration degree in the sample. The

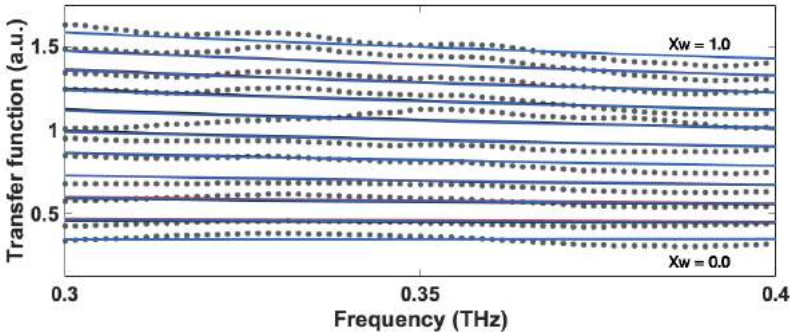

Figure 3.5: Experimental (grey dots) and theoretical (solid lines) transfer function of mixtures across the spectral band from 0.3 THz to 0.4 THz. Figure reprinted with permission from [113] © The Optical Society.

values predicted by MG, BM and LLL models in all the mixtures are shown in Table 3.3.

Mixture	MG	Δ	BM	Δ	LLL	Δ
1.0	1.01	0.01	1.01	0.01	1.01	0.01
0.9	0.92	0.02	0.92	0.02	0.92	0.02
0.8	0.81	0.01	0.81	0.01	0.81	0.01
0.7	0.71	0.01	0.71	0.01	0.71	0.01
0.6	0.60	0.00	0.60	0.00	0.60	0.00
0.5	0.47	0.03	0.47	0.03	0.47	0.03
0.4	0.38	0.02	0.38	0.02	0.38	0.02
0.3	0.27	0.03	0.27	0.03	0.27	0.03
0.2	0.21	0.01	0.20	0.00	0.20	0.00
0.1	0.09	0.01	0.08	0.02	0.08	0.02
0.0	0.00	0.00	0.00	0.00	0.00	0.00
Average		0.01		0.01		0.01

Table 3.3: Water volumetric fractions resulting from the least squares fitting of the MG, BM and LLL theoretical curves to the experimental data. The corresponding deltas are shown for the mixtures.

The results shown in Table 3.3, demonstrate that the outcome of all three models for the inverse problem are comparably good and acceptable with an average deviation of about 1%.

Model	Dielectric function	Guest particles shape	Symmetry
MG	Low contrast	Spherical	Asymmetric
BM	High contrast	Spherical	Symmetric
LLL	Low contrast	Arbitrary	Symmetric

Table 3.4: Key aspects of the MG, BM and LLL effective medium theory models.

A characteristic of biological tissue in the terahertz regime is the high contrast between the dielectric functions of water and the rest of the tissue, besides the variability in shape of the particles considered as background tissue. These factors together complicate the decision to select one model over another for the analysis of the optical properties for biological tissues. As summarized in Table 3.4, the MG theory restricts the particles to be spherical in shape, in addition it is asymmetric. BM model allows higher contrasts between dielectric functions of the components but it also restricts the particles to be spherical in shape. LLL model is a good choice if the mixture consists of irregularly shaped components, however, it is only, in principle, applicable if contrast in dielectric function of the components is limited, therefore biological tissue does not fully comply with the construction assumptions of any of them. The high contrast in the dielectric functions contradicts the hypothesis of the MG and LLL models, unlike the BM model that allows great differences in the permittivity. However, the shape of the dry tissue particles is irregular, this contradicts the hypotheses of the MG and BM models that are restricted to spherical particles, being the LLL model the only one among the considered models that allows arbitrarily shaped particles.

Overall, from the results shown in this comparison study, in spite of not fulfilling the construction hypothesis of the models, the three of them behave empirically well, fitting adequately the experimental data. Based on the fitting to the transfer function, all the three models are appropriate for the hydration quantification. From the calculation of the dielectric function error, the LLL and BM models are found to be more suitable for modeling biological tissue in the terahertz range.

Chapter 4

The Moisture MApping by Terahertz technique

Diabetes mellitus is nowadays considered a global pandemic owing to its high prevalence worldwide, affecting around 8% of the world population [114]. The prevalence of diabetes is rising alarmingly and figures in certain countries of the world have gone above 20% [115].

Diabetic foot syndrome is a long term consequence of diabetes mellitus. This condition causes ulceration in about 15% of cases [2] and such deterioration leads to amputation in about 2.5% of diabetic patients [3], diminishing their quality of life and generating extraordinary costs for patients and public health systems. Currently, there is no objective method for the detection of diabetic foot syndrome in its early stages. In this chapter, terahertz imaging as a method for the evaluation of the deterioration of diabetic foot syndrome is presented.

4.1 Diabetes and Diabetic Foot Syndrome

Diabetes occurs when the pancreas does not produce enough insulin or the insulin it produces is not used effectively by the body [116]. Insulin is a hormone that regulates blood sugar levels. Over time, high sugar levels cause severe damage to various organs and systems, especially the nerves and blood vessels [117]. The combination of microvascular and neurological deterioration causes diabetic foot syndrome. A patient with diabetic foot presents dehydration and loss of sensation in his/her feet [118]. Dehydrated skin becomes more fragile which favours the formation of ulcers than can become infected. Due to the loss of sensation, the capacity to notice the lesion is compromised and, if is not properly and timely treated, results in the partial or total amputation of the affected limb. This is the most common cause of non-traumatic amputations [119].

Due to the complexity and prevalence of this condition, an early diagnostic test to avoid these consequences is highly desirable. At present, the only strict definition of diabetic foot is that of "a foot affected by ulceration that is associated with neuropathy and/or peripheral arterial disease of the lower limb in a patient with diabetes" [120]. Unfortunately, this definition does not allow much room for early diagnosis, and is the consequence of the lack of an objective and quantitative screening method that allows preventive actions; at the same time such lack of an objective screening method has also made the assessment of preventive treatments difficult. The most used podiatric evaluation of diabetic patients before they present ulcers is a subjective test known as the monofilament that assesses the neurological deterioration [118]. This test consists of poking the feet of a blinded patient with a flexible tip and asking the patient to report when he/she feels the pressure, when the patient fails to report a number of pokes, the outcome of the test is considered to be positive [121]. Another indirect test is the ankle-brachial index, which uses Doppler ultrasound to compare the blood flow in arteries in the arm and ankle, which is an indicator of vascular deterioration [122].

4.2 Moisture MApping by Terahertz (MMAT)

Terahertz radiation is a highly sensitive, non-invasive, non-contact probe of the water content of materials. Assuming that deterioration of the skin of the feet of diabetics is a central element of their deterioration process, the Moisture MApping by Terahertz (MMAT) technique is proposed as a potential diagnostic tool for the diabetic foot syndrome. This technique consists of an imaging system, which we call MMAT scanner, and provides images of the water content in the feet soles as an objective indicator of skin deterioration and of the probability of developing ulcers. The MMAT technique, including the imaging scanner and the data processing is described in the following sections.

4.2.1 MMAT scanner

Most of the ulcers experienced by diabetic patients occur on the sole, in either the big toe, the metatarsal area or the heel area; therefore it is important to image the entire feet soles. Moreover, in order to extract the water content of tissue, spectral information is required. The MMAT scanner uses a terahertz time-domain imaging system that produces terahertz images of the foot sole.
The MMAT scanner consists of an elevated surface where a high-density polyethylene window, which is transparent at terahertz frequencies, is used to place the feet of the patient. A chair is also provided in order to maintain the patient comfortably in position and avoid motion of the feet during the image acquisition. The space under the patient sitting area is used to place a terahertz time-domain imaging system, which is used to produce the image from underneath.

MMAT scanner v1

An appropriate equipment for the acquisition of feet sole images was designed and implemented as a first version of the MMAT scanner, shown in Figure 4.1. A platform was built to maintain the subject in a sitting position, while his/her feet rested on two high-density polyethylene windows. The terahertz time-domain imaging system consisted of a Menlo TeraK15 spectrometer interfaced with a couple of linear translation stages. The terahertz spectrometer was based on an Er:fiber laser which produced 90 fs pulses at a repetition rate of 100 MHz. The THz-TDS emitter and detector were placed on a mount to keep them forming a 12.5° "pitch-catch" geometry. The mount was placed on the pair of orthogonally aligned translation stages which were in turn positioned on a plate parallel to the polyethylene windows. One polyethylene window was scanned to produce a terahertz image of the right foot sole. The terahertz image consisted of a collection of terahertz waveforms taken across a 22 x 54 points area spaced by 5 mm. The scanning time was of approximately 40 minutes for one foot.

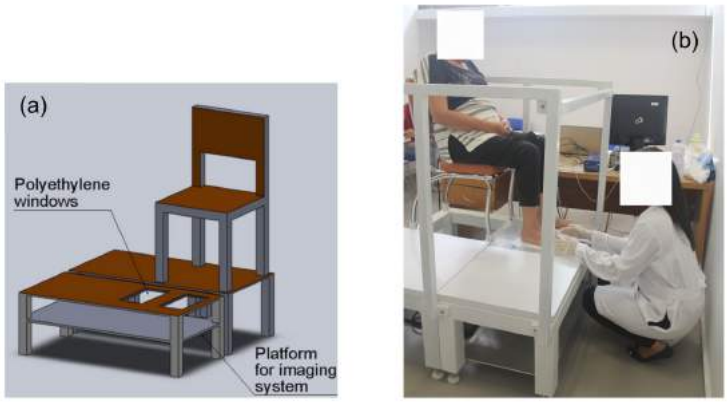

Figure 4.1: MMAT scanner v1. (a) Platform setup design considering a chair, two polyethylene windows and a platform for the imaging system. (b) Terahertz images acquisition during the MMAT technique proof-of-concept study.

This first version of the MMAT scanner was used to perform a proof-of-concept study of the MMAT technique [100]. Terahertz images of the right foot of diabetic patients and non-diabetic subjects were acquired, Fig.4.2. Subsequently, the data were processed and images were formed with the information of the skin hydration pixel by pixel. The results reported demonstrate that there are significant differences between the hydration of the feet of subjects in the control and diabetic groups. Nevertheless, this study was initially proposed as a technical test of the equipment and, therefore, many formal requirements of a clinical trail were not met in the acquisition of the data presented. For instance, the size of the sample was insufficient, the subjects in the control group did not undergo a reference test, and finally there was a significant difference in the average age of the control and diabetic groups, which could result in statistical bias of the observations. Yet, the results were encouraging and provided key elements for the design of a clinical trial, which is presented in Chapter 6. Moreover, the data acquired from this study were used to form an additional image display to show areas with risk of ulceration. This approach is further described in Chapter 5.

MMAT scanner v2

Having performed the proof-of-concept study, a second scanner, Figure 4.2 (a), was designed to improve the platform and the imaging capabilities. The terahertz time-domain imaging system, placed below the measurement window, Fig. 4.2 (b), is an API TeraGauge spectrometer coupled to an API Imaging Platform. The terahertz time-domain spectrometer is based on a Yb:Fiber laser which produces ultrashort pulses at a repetition rate of 1 KHz. The THz-TDS transmitter and receiver are coupled with a collinear adapter to form a normal reflection transceiver, Figure 4.3 (a). The collinear adapter is mounted on the imaging platform which consists of rails and motion controllers to perform raster scans. The full polyethylene window is scanned to produce the terahertz image which consists of a collection of terahertz waveforms taken across a 240

x 245 points area spaced by 1 mm. Both feet soles are imaged in the same scan in approximately 10 minutes.

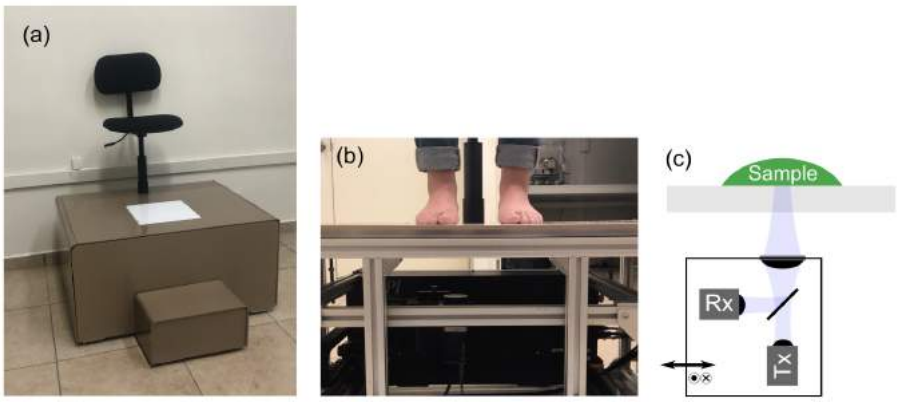

Figure 4.2: MMAT scanner v2. (a) Platform with an elevated surface, a high-density polyethylene window (white) is used to placed the patient's feet, the chair maintains the patient in position. (b) The terahertz imaging system scans the window from underneath. (c) The transmitter (Tx) and receiver (Rx) are coupled by an adapter to perform as collinear reflection transceiver.

4.2.2 MMAT images

The MMAT technique provides quantitative information of the water content in the skin displayed as hydration- and color-coded-images. Hydration-images provide a water content mapping as a quantitative indicator of the deterioration in the feet. The color-coded-images provide objective identification of areas with low hydration and higher ulceration risk. In addition, a number of quantitative and punctual parameters can be obtained from the images such as the average hydration of the feet, the hydration at certain regions of interest, and the low/high risk areas fraction on the feet. The raw data of each terahertz image is processed in order to obtain the water content of the skin at each point of the image as described in the following section. The data processing for the color-coded-images will be further described in Chapter 5.

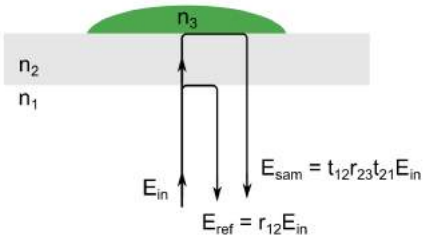

Figure 4.3: Ray schematic of the terahertz radiation path in THz-TDS normal reflection geometry. The input THz signal splits into a reference and a sample signal. The output signals are described by the input THz signal, and the transmission and reflection at the interfaces.

In order to obtain the water content in each pixel of the terahertz image, the reflected terahertz radiation is analyzed by comparing the experimental reflection transfer function with the analogous theoretically modeled reflection transfer function.

Following the analysis provided in Section 2.2 for the terahertz radiation propagation illustrated in Fig. 4.3 (b), the experimental reflection transfer function is obtained as

$$\mathrm{R}_{\mathrm{exp}}(\omega) = \left| \frac{\tilde{\mathrm{E}}_{\mathrm{sam}}(\omega)}{\tilde{\mathrm{E}}_{\mathrm{ref}}(\omega)} \right|. \tag{4.1}$$

Subsequently, the theoretical reflection transfer function is described in terms of the Fresnel reflection coefficients considering the calibration factor and given by

$$\mathrm{R}_{\mathrm{theo}}(\omega, \eta) = \frac{\mathrm{r}_{23,\mathrm{sam}}(\omega, \eta)}{\mathrm{r}_{23,\mathrm{air}}} \mathrm{R}_{\mathrm{air}}(\omega), \tag{4.2}$$

where $\mathrm{r}_{23,\mathrm{sam}}(\omega, \eta)$ is the Fresnel reflection from the skin as a function of the water content η, $\mathrm{r}_{23,\mathrm{air}}$ is the reflection coefficient when air is in contact with the measurement window, and $\mathrm{R}_{\mathrm{air}}$ is the air reflection transfer function given by

$$\mathrm{R}_{\mathrm{air}}(\omega) = \left| \frac{\tilde{\mathrm{E}}_{\mathrm{air}}(\omega)}{\tilde{\mathrm{E}}_{\mathrm{ref}}(\omega)} \right|. \tag{4.3}$$

For normal incidence, the Fresnel reflection coefficients are given by

$$\mathrm{r}_{23,\mathrm{air}} = \frac{1 - \mathrm{n}_{\mathrm{HDPE}}}{1 + \mathrm{n}_{\mathrm{HDPE}}} \tag{4.4}$$

and

$$\mathrm{r}_{23,\mathrm{sam}}(\omega, \eta) = \frac{\mathrm{n}_{\mathrm{HDPE}} - \tilde{\mathrm{n}}_{\mathrm{skin}}(\omega, \eta)}{\mathrm{n}_{\mathrm{HDPE}} + \tilde{\mathrm{n}}_{\mathrm{skin}}(\omega, \eta)}, \tag{4.5}$$

where the refractive index of the polyethylene window $\mathrm{n}_{\mathrm{HDPE}}$ is constant and known in practice, and the complex refractive index of the skin $\tilde{\mathrm{n}}_{\mathrm{skin}}$ is given by

$$\tilde{\mathrm{n}}_{\mathrm{skin}}(\omega, \eta) = \sqrt{\varepsilon_{\mathrm{mix}}(\omega, \eta)} \tag{4.6}$$

where $\varepsilon_{\mathrm{mix}}(\omega, \eta)$ is the dielectric function of human skin determined by the LLL model of effective medium theory [107] considered as a combination of water and dry skin,

$$\sqrt[3]{\varepsilon_{\mathrm{mix}}(\omega, \eta)} = \eta \sqrt[3]{\varepsilon_{\mathrm{water}}(\omega)} + (1 - \eta) \sqrt[3]{\varepsilon_{\mathrm{dry\,skin}}(\omega)}, \tag{4.7}$$

the dielectric function of water, $\varepsilon_{\mathrm{water}}$, is well known for terahertz frequencies [101] and the dielectric function of dry skin, $\varepsilon_{\mathrm{dry\,skin}}$, was obtained from Ref. [100]. Finally, the water content at each measured point is determined by minimizing the difference between the experimental and theoretical reflection transfer functions by varying the parameter η in a least square fitting algorithm and, "hydration images", are formed with the water content information.

Chapter 5

RYG-color-coded images

The proposed MMAT technique provides hydration images which map the water content in the feet soles of diabetic patients as an objective indicator of the skin deterioration. Nevertheless, although significant differences can be observed regarding the water content, it is still necessary to define indicators to perform a better diagnosis of the syndrome, follow up the treatments given to the patients, and help in the prevention of injuries. Moreover, the hydration images are relatively hard to interpret, with the exception of extremely dehydrated or extremely well-hydrated feet soles. In order to overcome these limitations and simplify the interpretation of the images, a new form of image display is proposed that shows the clearly distinguished areas of the foot sole in three different colors depending on the degree of hydration: red for low hydration, yellow for medium hydration, and green for good hydration which, in turn, indicate the degree of deterioration as high-, medium-, and low-risk, respectively.

5.1 RYG-image construction

The right foot of a group of 38 diagnosed diabetic patients from the *Hospital Regional León* of the *Instituto de Seguridad y Servicios Sociales de los Trabajadores del Estado* was imaged with one exception, which was a patient that already had undergone right-foot amputation, in that case, the left foot was imaged instead. Of the images taken, 26 were discarded because they were unsuitable for analysis, mainly because the patient moved during the data acquisition. In addition, 33 volunteers were recruited among students and employees of the *Centro de Investigaciones en Óptica A. C.*; none of them was diagnosed diabetic, however, no control test was applied to this group. Of those images, 12 were discarded following the same criteria as for the diabetic patients. The terahertz images of the diabetic and control subjects were acquired using the MMAT scanner v1, and the pixel-by-pixel water content was determined by least square fitting on the reflection transfer function as described in Section 2.2 and Section 4.2.2.

The proposed RYG-color-coded (red yellow green) images are constructed based on the sensitivity and specificity values of the diagnostic test. Sensitivity indicates the probability of correctly identify the diseased subjects, and is defined as

$$\text{Sensitivity} = \frac{\text{True positives}}{\text{True positives} + \text{False negatives}}, \tag{5.1}$$

whereas specificity, which identifies the non-diseased subjects, is given by

$$\text{Specificity} = \frac{\text{True negatives}}{\text{True negatives} + \text{False positives}}. \tag{5.2}$$

True positives, false negatives, true negatives and false positives values are determined in a 2x2 contingency table, Table 5.1, according to the results given by the diagnostic test and a golden standard.

	Golden standard result	
Diagnostic test result	Diseased	Non-diseased
Positive	True positives	False positives
Negative	False negatives	True negatives

Table 5.1: 2x2 contingency table. Diagnostic test result in relation to the golden standard result. Subjects with diagnostic test values less than the threshold are classified as positive and subjects with diagnostic test values greater than or equal to the threshold are classified as negative.

Currently there is not a proper golden standard for *early* diabetic foot syndrome, therefore all the diagnosed diabetics were taken as true positives, as a first approximation. The threshold values to consider the test as positive were found by plotting sensitivity and specificity as a function of the threshold value used to separate negative and positive outcomes of the test, as shown in Figure 5.1. Since the population shows a normal distribution, and therefore the sensitivity and specificity show an error-function-like behaviour, such functions were fitted to the datasets and are shown in the plots.

In order to determine the threshold values that guarantee both a sensitivity and a specificity larger than 0.95, the lowest threshold that gives such specificity (47.0%, (d) in Fig. 5.1) and the highest threshold that gives that sensitivity (55.8%, (f) in Fig. 5.1) were found. The RYG images were constructed in such a way that pixels with water volumetric fractions below 47.0% were colored in red, pixels with water volumetric fractions above 55.8% were colored in green, and pixels with a water volumetric fraction in between were colored in yellow. RYG-color-coded images of diabetic and non-diabetic subjects are represented in Figure 5.2.

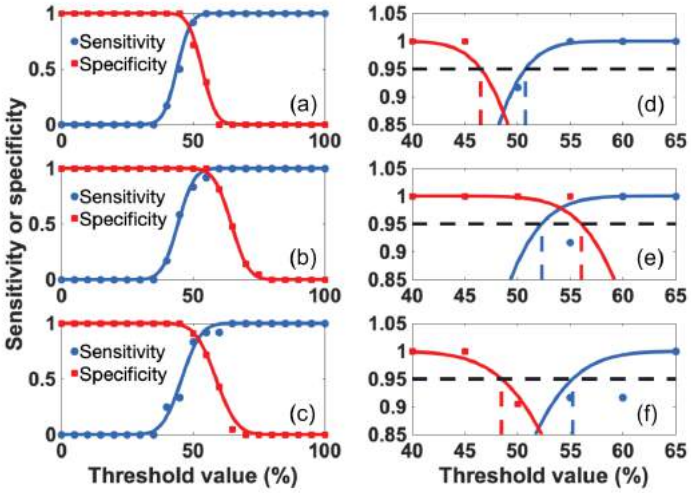

Figure 5.1: Sensitivity (blue circles) and specificity (red squares) values for the tests of average humidity across the sole of the foot (a), humidity in the big toe (b), and humidity in the center of the heel (c) with respect to the variation in the threshold (humidity percentage). Zoom in 95% for sensitivity (blue) and specificity (red) in order to define a hydration threshold from the three tests: average humidity (d), humidity in the big toe (e), and humidity in the center of the heel (f). Figure reprinted with permission from [123] © Springer Nature.

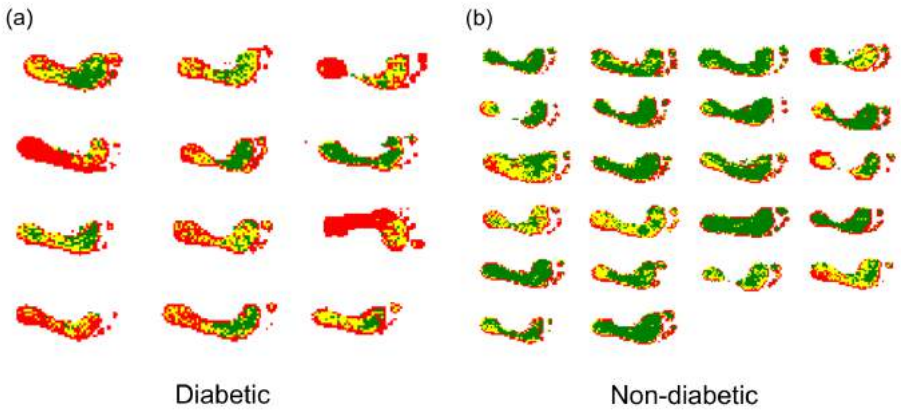

Figure 5.2: RYG images show the foot of (a) diabetic patients and (b) non-diabetic subjects in three different colors: red for hydration below 47.0%, yellow for hydration between 47% and 55.8%, and green for hydration above 55.8%. There is a clear distinction between the two groups. Figure reprinted with permission from [123] © Springer Nature.

From Figure 5.2 it is noticeable that the differences between both groups are significant, a large proportion of the control group has mostly green pixels with relatively small areas in red, and in comparison, almost all diabetics show a relatively small fraction of green pixels, and some of them have very significant fraction of the sole classified as red. Furthermore, it is easy to identify that some diabetic patients in Fig. 5.2 (a) present a proportion of the feet surface with a deterioration larger than the rest of the diabetic group. With a careful analysis of the RYG images it is also observable that almost all diabetics show red areas in their heels and toes, which is consistent with the areas where diabetics commonly develop ulcers; therefore, it is possible to foresee that a scheme similar to this one could have the potential in order to predict areas at risk of developing ulcers before they actually appear.

5.2 Pixel statistical analysis

In order to have a more quantitative idea of how the RYG-color scheme separates the control and diabetic groups, statistics of the fraction of pixels that meet each of the three hydration conditions were performed to identify if this could provide an additional quantitative indicator to help the diagnostician. The percentage occupied by each of the colors (red, yellow, and green) in the sole of the foot of the diabetic and non-diabetics subjects was obtained. The values are shown in Figure 5.3. While there is a clear difference in the proportion of red and green pixels between the two groups, the fraction of yellow pixels seems to be statistically similar between the two groups. It is worth pointing out that all non-diabetics have under 45% of red pixels, while two thirds of the diabetic patients have over 45% of red pixels. Analogously, all non-diabetic images have more than 18% of their pixels in green, while over half of the diabetics' images have lees than 18% of their pixels classified as green.

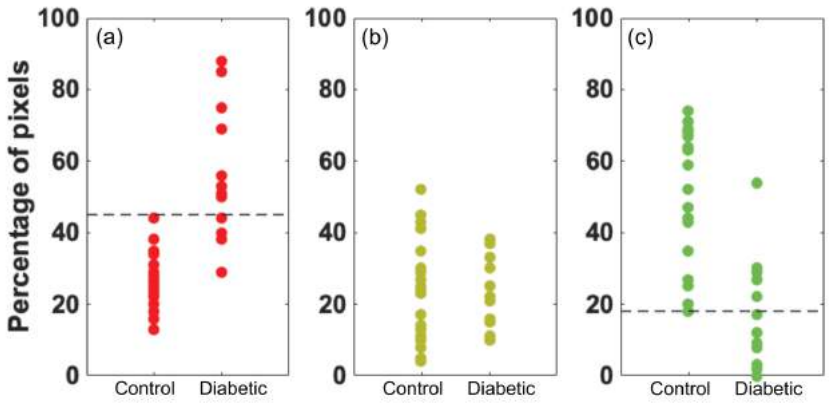

Figure 5.3: The percentage of occupation of each color in the sole of the foot of the diabetic and control (non-diabetic) subjects is shown in each of the three graphs. It can be seen that diabetic patients present, statistically, higher percentage of red pixels (a) and lower percentage of regions of green pixels (c) than non-diabetics. Both groups show similar percentages of yellow pixels (b). Figure reprinted with permission from [123] © Springer Nature.

An additional indicator of the level of deterioration is the difference of the fraction of green and red pixels defined as

$$\mathrm{G} - \mathrm{R} = \%\,\mathrm{Green\,pixels} - \%\,\mathrm{Red\,pixels}. \tag{5.3}$$

Such difference is presented in Figure 5.4 for all subjects of both groups. The plot shows that all non-diabetics have a $\mathrm{G} - \mathrm{R}$ difference higher than -18%; taking this as a threshold, 82% of the diabetics show a $\mathrm{G} - \mathrm{R}$ difference below that.

Together, these studies indicate that terahertz imaging is a potential screening method for early stages of feet deterioration in diabetic patients. From the amount of water in different regions of the sole of the foot, quantitative indicators of the degree of deterioration of the skin can be determined and with it, the risk of developing an ulcer. The RYG images allow a better visualization of

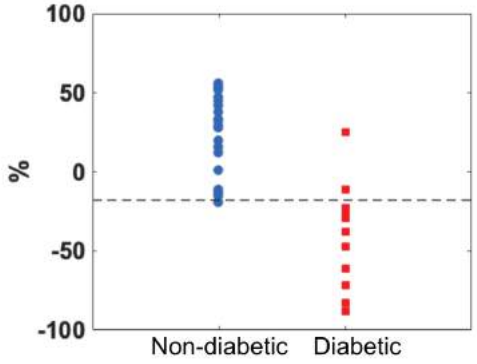

Figure 5.4: G − R difference obtained by subtracting the percentage of red pixels from the percentage of green pixels. Non-diabetic subjects (circles) present G − R values between -18% and +65% while diabetic patients (squares) are all bellow +30% and more than 4/5 of them are below -18%. The dashed line is located along the -18% level to visualize the separation between groups. Figure reprinted with permission from [123] © Springer Nature.

regions of interest, that is, areas on the sole of the foot with larger risk level. In addition, they help the diagnostician to determine the severity and extent of the diabetic foot problem. The statistics of the number of red, yellow, and green pixels in conjunction to the absolute hydration values serve as quantitative measures of the problem and can therefore be used in the evaluation of the patients' evolution and the assessment of new treatments. While encouraging, it is worth mentioning that these RYG images resulted from the proof-of-concept study and therefore are limited by the lack of a golden standard for early diabetic foot deterioration, the age difference between the groups of subjects and the sample size. Notwithstanding these limitations, this color-coded images concept is proposed to be implemented, together with the hydration images, for the early diagnosis of diabetic foot syndrome by terahertz imaging.

Chapter 6

MMAT clinical test

A first test was realized using the MMAT technique following the formal requirements of a clinical trail. Terahertz images of the feet soles of diabetic and non-diabetic subjects were acquired. Golden standard tests were performed to assure the presence/absence of diabetes. Moreover, diabetic patients were tested for neurological and microvascular deterioration. A comparison between diabetic and non-diabetic subjects is presented as a normality study of the proposed diagnostic test. Subsequently, considering the golden standard tests and the MMAT results, diabetic patients are classified according to the complications related to diabetic foot syndrome. Finally, an analysis on the test potential is presented and the sensitivity, specificity and threshold values of the MMAT technique are defined.

Subjects imaging

A total of 80 diabetic and 100 non-diabetic (control) subjects were studied. Diabetic patients were recruited from the *"DiabetIMSS"* program at the *"Instituto Mexicano del Seguro Social"* (IMSS). The control group was recruited among patients and relatives from a waiting room at the *"Unidad Médica de Alta Especialidad"* (UMAE) IMSS-T1. All control subjects underwent a quick glucose

test with a commercial glucometer to verify the absence of diabetes. Of all the diabetic patients, 60 were tested for peripheral diabetic neuropathy (PAD) with a Semmes Weinstein monofilament (SWM) and 59 for peripheral artery disease (PAD) by the ankle-brachial index (ABI). All diabetic patients were requested in advance not to apply any moisturizing products before the image acquisition. This same instruction was not given to the control subjects since they were chosen randomly, yet, information about the application of moisturizing products on the feet was collected for future consideration. The terahertz images were acquired with the MMAT scanner v2. The measurement window was cleaned up with isopropanol before both feet were placed for the image acquisition. Both feet soles of all subjects were scanned with terahertz time-domain imaging and, additional personal and clinical data relevant to the study were collected. The scanning time was approximately 10 min. The raw data from the terahertz images were analyzed as detailed described in Chapter 4, Section 4.2.2 to retrieve the water content in the skin at each measured point. The procedure of the study is illustrated in Figure 6.1.

Figure 6.1: MMAT clinical study procedure. All subjects were informed about the study and, personal and clinical data were collected, golden standard tests were performed, and finally, the terahertz image was acquired.

Hydration evolution with age

As part of the conclusions of the MMAT technique proof-of-concept study, it was suggested that age might play an important role on the skin hydration and hence in the differences between diabetic and non-diabetic subjects [100]. To overcome this bias, the volunteers of this clinical test were recruited to meet a wide age range. The age of the control subjects ranged from 20 to 85 years, whereas the diabetic patients were within 40 and 85 years old. The evolution of the water content in the skin with age was analyzed. Control subjects were divided into two age groups, older than 20 years and older than 40 years. The relationship between hydration and age is shown in Figure 6.2. Data points represent the hydration averaged over each and all the soles of the subjects. Linear fits to the data are represented by solid lines. The confidence intervals of the fits, which in turn denote the trend uncertainty, are represented by the shaded areas.

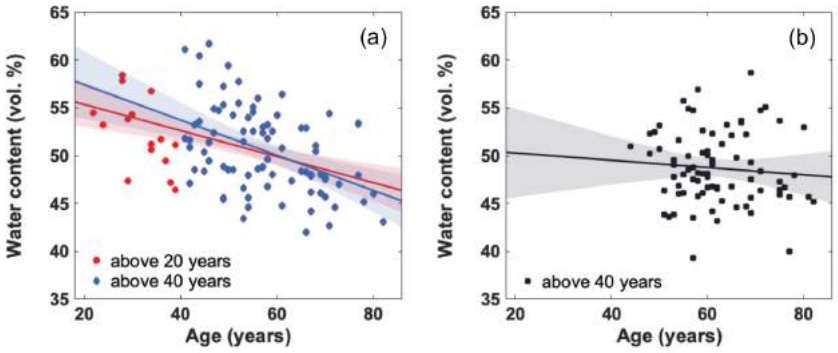

Figure 6.2: Average foot sole hydration evolution with age on (a) control subjects above 20 years (red circles, n = 98, r = −0.4235, p = 1.39e^{-5}) and above 40 years (blue diamonds, n = 83, r = −0.4409, p = 3.03e^{-5}), and on (b) diabetic subjects above 40 years old (black squares, n = 79, r = −0.0875, p = 0.4434), n denotes the number of subjects per group and p the p-value of the data sets. Linear fits to data and confidence intervals are represented by solid lines and shaded areas, respectively.

The large slope uncertainties, suggest that a lineal model is only indicative but perhaps is not the most appropriate. Nevertheless, it is noticeable that young (below 40 years) non-diabetic subjects present higher hydration values than older control subjects and diabetic patients. To determine the relationship between age and the skin water content, the Pearson correlation coefficient r was calculated for each data set, together with the corresponding correlation Student t-Test (p-value) considering a significance value of $\alpha = 0.05$. It is worth mentioning that the p-value should be smaller than the significance value in order to consider the correlation to be valid. The calculated p-value of the diabetic patients data, $p = 0.4434$, is much greater than the significance value, denoting that there is no correlation between age and the water content in the skin of diabetic patients. On the other hand, the p-values of the control subjects above 20 and 40 years, $p = 1.39e^{-5}$ and $p = 3.03e^{-5}$, respectively, are smaller than the significance level, indicating that although moderate there is tendency of the skin to dehydrate with age.

6.1 Normality study: non-diabetic vs. diabetic subjects

From the total of volunteers, 53 control and 40 diabetic subjects in the age range from 40 to 60 years were considered for a normality study. The water content averaged over the foot sole, at the center of the big toe and at the center of the heel was obtained. The hydration values from both feet of each volunteer were averaged. Figure 6.3 shows the hydration distribution for diabetic and non-diabetic subjects (a) averaged over the foot sole, (b) at the center of the big toe and (c) at the center of the heel. The box represents the middle 50% of the data, 25% of the data are below the lower bar (Q1), the middle bar represents the median (Q2) and 75% of the data rely below the upper bar (Q3). The variability of the data or interquartile range (IQR), is measured by the difference between the upper and lower bars as $IQR = Q3 - Q1$. Data

values smaller than $Q1 - 1.5\,IQR$ or greater than $Q3 + 1.5\,IQR$ are considered as outliers. The data significance was determined by performing an analysis of variance (ANOVA test) to calculate the p-value. The smaller the p-value the more significant the data.

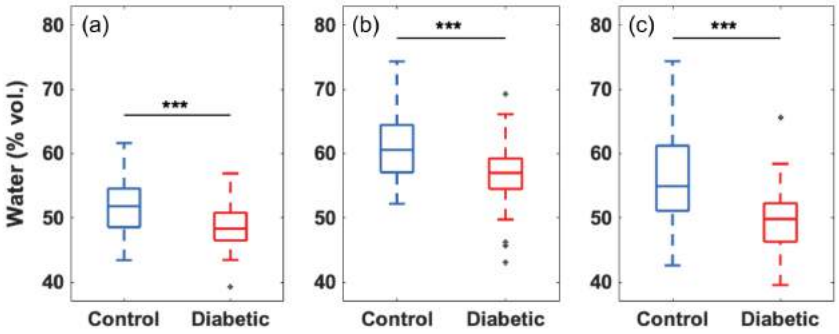

Figure 6.3: Skin hydration distribution (a) averaged over the foot sole ($p = 5.90e^{-4}$), (b) at the center of the big toe ($p = 4.30e^{-4}$), and (c) at the center of the heel ($p = 8.70e^{-6}$) of control ($n = 53$) and diabetic ($n = 40$) subjects. The dark grey crosses indicate the outliers and the statistical significance is denoted by black asterisks displayed over the boxplots (* for $p \leq 0.05$, ** for $p \leq 0.01$, and *** for $p \leq 0.001$).

From Fig. 6.3, we can see that, control subjects' hydration values are above diabetics' hydration values. The largest separation between groups is given by the hydration at the center of the heel (Fig. 6.3 (c)).

6.2 Diabetic subjects' classification

Diabetic patients were classified according to the complications associated to the diabetic foot syndrome. Since diabetic foot is defined as "a foot affected by ulceration that is associated with neuropathy and/or peripheral arterial disease of the lower limb in a patient with diabetes" [120], diabetic patients with neuropathy and/or ulceration- and/or amputation- record were considered as diabetics with complications, being diabetic patients without neuropathy nor

ulceration nor amputations considered as diabetics with no complications.
In order to evaluate neuropathy, the monofilament test was performed in 60 diabetic patients. Neuropathy was diagnosed in patients who scored less than 8 out of 10 monofilament points. Taking these tests results and the ulcers/amputation records, from all the 80 diabetic patients, only 45 were considered in the "diabetics with no complications" group and 21 in the "diabetics with complications" group. In Figure 6.4, a terahertz hydration image of (a) a diabetic patient with no complications and of (b) a diabetic patient with complications can be observed. The terahertz hydration image in Fig.6.4 (b) corresponds to a diabetic patient with an ulcer in the right metatarsal area, indicated by a red arrow. During the terahertz scanning, the ulcer was covered by a patch, therefore the water content information was not obtained for this region. The skin hydration

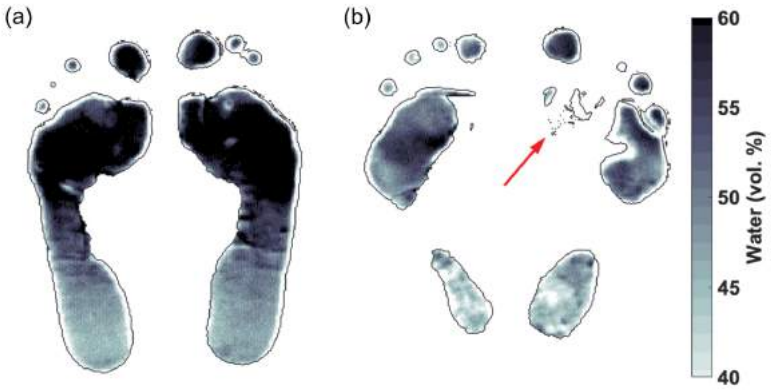

Figure 6.4: Hydration image of (a) diabetic patient with no complications and (b) diabetic patient with complications. An ulcer, covered by a patch (indicated by the red arrow), is noticeable on the right metatarsal area of the diabetic patient with complications which, in turn, presents lower hydration along the foot sole compared to the diabetic patient with no complications.

is represented as a greyish color map ranging from 40% to 60%. For water content below 40% the color map is fixed to white in order to highlight highly dehydrated skin. For water content above 60% the color map is fixed to black to highlight skin highly hydrated.

It has been established that terahertz hydration images give information of the water content pixel by pixel along the foot sole, but if the water content of the skin is color-coded and Red-Yellow-Green (RYG) images [123] are formed, it is possible to easily visualize areas with high risk of ulceration. Analogously to the analysis described in Chapter 5, Section 5.1, hydration thresholds were defined to color-coding water content information. RYG-images were formed in which pixels below 51.7% were colored in red, pixels above 52.9% were colored in green and pixels with values in between were colored in yellow. In Figure 6.5, RYG images of (a) a diabetic patient with no complications and (b) a diabetic patient with complications are shown as examples. We can notice that even though the

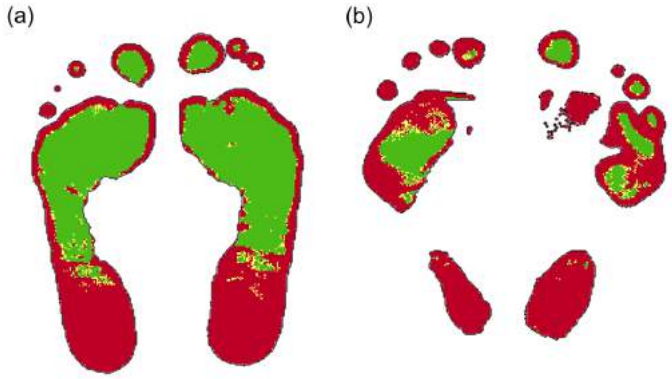

Figure 6.5: RYG-images of a (a) diabetic patient with no complications and a (b) diabetic patient with complications. Red pixels, colored for hydration values below 51.7% indicate high ulceration risk. Green pixels, colored for hydration values above 52.9%, denote low ulceration risk. Yellow pixels are colored for hydration values in between. Diabetic patients with complications present more high-deterioration-risk areas than the diabetic patients with no complications.

diabetic patient with no complications presents high ulceration risk areas, they represent a significantly smaller fraction of the foot-sole area than those of the diabetic patient with complications feet. Furthermore, we can observe that the area surrounding the ulcer in the right metatarsal of the diabetic with complications is highly deteriorated and so colored in red.

The average hydration and the green pixels and red pixels distribution over the foot sole of the diabetic subjects in both groups were obtained from the hydration- and RYG-images. The values of feet with ulcers and/or amputations were not considered, i.e., if a diabetic patient had had an ulcer or had already undergone an amputation on one of his/her feet, the opposite-foot values were taken into account for this study. The distribution of the hydration and pixels fraction values can be observed in Figure 6.6 (a)-(c). The data distribution and outliers are displayed as described in Section 6.1. The data significance was determined performing an ANOVA test to calculate the p-value.

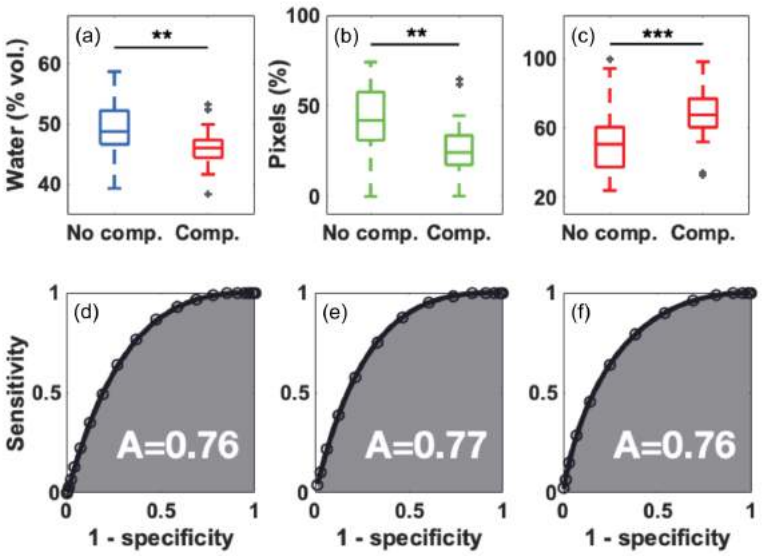

Figure 6.6: (a) Hydration averaged over the foot sole ($p = 0.0016$), (b) green pixels ($p = 0.0011$) and (c) red pixels ($p = 0.001$) distribution of diabetic subjects with no complications (n=45) and with complications (n=21). Diabetic patients with complications present the less hydration values and green pixels fraction and the more red pixels fraction than diabetic patients with no complications. The dark grey crosses indicate the outliers and the statistical significance is denoted by black asterisks displayed over the boxplots (* for $p \leq 0.05$, ** for $p \leq 0.01$, and *** for $p \leq 0.001$). The (d), (e), and (f) ROC curves indicate the ability to discriminate between both diabetic patients groups accordingly to (a), (b), and (c), respectively.

From Fig.6.6 (a) we can see that the average hydration in the foot sole of diabetic patients with no complications is higher than of diabetic patients with complications. Additionally, the fraction of green pixels (Fig. 6.6 (b)) and red pixels (Fig. 6.6 (c)) is larger and smaller, respectively, in diabetic patients with no complications than in diabetic patients with complications.

The potential of a test to diagnose a disease is represented by a Receiver Operating Characteristic (ROC) curve [124, 125]. A ROC curve is constructed from the sensitivity and specificity values of the diagnostic test. Sensitivity and specificity are determined by Eq. 5.1 and Eq. 5.2, respectively. Subsequently, sensitivity and specificity curves as function of the threshold are calculated as described in Chapter 5, Section 5.1 and the ROC curve is given by plotting sensitivity against (1-specificity). The area under the ROC curve is determined as an indicator of the overall potential of the test, the larger the area under the ROC curve, the better the diagnosis potential of the test. Consequently, considering the hydration values and the green- and red-pixels distribution over the foot sole, ROC curves were determined to represent the potential of the MMAT test to discriminate between diabetic patients with complications and diabetic patients with no complications. These ROC curves can be observed in Fig. 6.6 (d)-(f). The areas under the corresponding ROC curves, indicate that, the averaged hydration, and the green pixels and red pixels distribution values have the potential to classify diabetic patients according to the complications associated to the diabetic foot syndrome.

Peripheral arterial disease and hydration in the skin

As previously mentioned, currently diabetic foot is partly diagnosed evaluating the vascular deterioration or peripheral arterial disease (PAD) by the ankle-brachial index (ABI). During the MMAT clinical trial, 59 diabetic patients were tested for PAD by ABI. Subsequently, the ABI results were compared to the water content averaged over the feet soles of the diabetic patients, as shown in Figure 6.7.

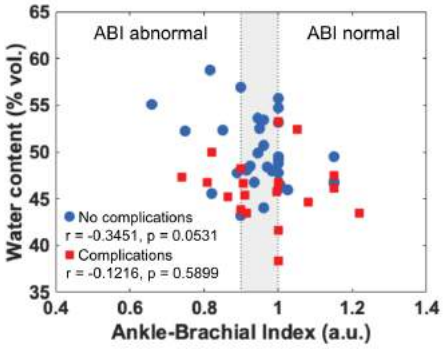

Figure 6.7: Water content averaged over the foot sole with respect to the ankle-brachial index (ABI) for diabetic patients with complications (red squares, n=22) and diabetic patients with no complications (blue circles, n=32). The grey shaded area indicates ABI "borderline" values (0.91 to 0.99), ABI values $\leq$ 0.90 are considered abnormal, the ABI normal range is defined from 1.0 to 1.40.

Peripheral arterial disease is diagnosed for ABI values $\leq$ 0.90 [126]. From the Pearson correlation coefficients r and p-values (t-Test) displayed in Fig. 6.7, it can be observed that there is no correlation between the vascular deterioration and the skin hydration in the foot in either the diabetic patients with complications and the diabetic patients with no complications. This suggests that the skin dehydration in diabetic patients is not related to a vascular deterioration but to a nervous one. The nervous system, particularly the sympathetic nervous system, regulates the sweating [127]. Therefore, dehydration of the skin could be due to alterations in the sympathetic nervous system's control of sweating. Given this observation, ABI results were not considered for the MMAT analysis.

6.3 Diagnostic test analysis

The diagnosis potential of a medical test is measured by its sensitivity and specificity values. These values can be determined by defining a threshold value to consider the outcome of the test as positive or negative and diagnosing the subjects under study into diseased and non-diseased. Together with the golden standard test result, the subjects are classified in a 2x2 contingency table, Table 5.1, as true positives, false positives, false negatives and true negatives as follows. *True positives*: diseased subjects correctly identified as diseased. *False positives*: non-diseased subjects incorrectly identified as diseased. *True negatives*: non-diseased subjects correctly identified as non-diseased. *False negatives*: diseased subjects incorrectly identified as non-diseased. Finally, once all the subjects are classified, sensitivity and specificity values are determined by Eq. 5.1 and Eq. 5.2. This procedure is true when the threshold value is well defined. If it is of interest finding the optimal threshold value in order to get the highest sensitivity and specificity of the diagnostic test at the same time, an analysis on the ROC curves may be performed.

In order to evaluate the capability of the MMAT diagnostic test to accurately classify diabetic patients as diseased or non-diseased, a ROC analysis was performed as detailed in Refs. [124, 125]. It is worth recalling that the aim of this study is to diagnose diabetic foot syndrome which is characterised by ulceration associated with neuropathy, therefore, 2x2 contingency tables were built considering as golden standard the results from the monofilament test together with the ulcers/amputations record. Three threshold values for the diagnostic test were defined in terms of the water content in the skin and, the red and green pixels fraction over the foot sole. The threshold values were varied within 0 and 100 percentage points, contingency tables were constructed for each threshold value, and sensitivity and specificity values were calculated to plot the corresponding ROC curves. The area under the ROC curve was determined. Finally, for each diagnostic test, the optimal threshold value was found by minimizing

the Euclidean index [128] given by

$$d^2 = (1 - \text{sens.})^2 + (1 - \text{spec.})^2, \tag{6.1}$$

and then by optimizing the resulting threshold value for a higher sensitivity value.

From the 2x2 contingency table, positive and negative predictive values can also be obtained. The positive predictive value (PPV) denotes the probability of the disease to be present when the test is positive and is given by

$$\text{PPV} = \frac{\text{True positives}}{\text{True positives} + \text{False positives}}. \tag{6.2}$$

The negative predictive value (NPV) is the probability that the disease is not present when the test is negative and is defined as

$$\text{NPV} = \frac{\text{True negatives}}{\text{True negatives} + \text{False negatives}}. \tag{6.3}$$

It is worth mentioning that PPV and NPV are dependent on the prevalence of the disease among the subjects under study [125].
Together with the sensitivity, specificity and threshold values, the PPV and NPV for the average hydration, and green- and red-pixels fraction tests were calculated. The MMAT diagnostic values are summarized in Table 6.1.

	Average	**Green**	**Red**
Sensitivity	81%	76%	76%
Specificity	69%	73%	78%
PPV (*)	55%	57%	62%
NPV (*)	89%	87%	88%
Threshold	47.6%	32.5%	61.5%

Table 6.1: Sensitivity, specificity, positive and negative predictive values, and threshold values of the MMAT diagnostic test regarding the average foot sole hydration and, green pixels and red pixels distribution. (*) These values are dependent on the disease prevalence.

Overall, the MMAT test for diagnosing diabetic foot shows that,

- MMAT hydration-images diagnose diabetic foot syndrome with a sensitivity of 81% and a specificity of 69% according to the average water content over the foot sole. The hydration threshold to be tested as positive or negative is 47.6%.
- MMAT RYG-images diagnose diabetic foot syndrome with a sensitivity of 76% and a specificity of 73% according to the green pixels fraction which threshold value is set at 32.5%.
- MMAT RYG-images diagnose diabetic foot syndrome with a sensitivity of 76% and a specificity of 78% according to the red pixels fraction which threshold value is set at 61.5%.

These diagnostic test analysis results suggest that the MMAT technique has the potential to identify diabetic patients with complications related to the diabetic foot syndrome. The sensitivity and specificity values estimated in the range from 76% to 81% and 69% to 78%, respectively, are encouraging for an early, non-invasive, objective and direct diabetic foot diagnostic test.

Chapter 7

Conclusions

This thesis reports on the medical applications of terahertz radiation, particularly the introduction of a terahertz-imaging technique for the early diagnosis of diabetic foot syndrome named Moisture MApping by Terahertz. Furthermore, an important part of this work is the comparative study of effective medium theory models, used for the quantification of water content in biological tissue. The results obtained indicate that the three models compared qualitatively fit the experimental data. A quantitative analysis was made by calculating the error between experimental and theoretical data, as well as by using least squares adjustments of the experimental data by the three models, from this we concluded that the Landau-Lifshitz-Looyenga and Bruggeman theories are quantitatively the more suitable for modeling biological tissues in the terahertz regime.

The Moisture MApping by Terahertz (MMAT) technique was presented as a potential tool for the early diagnosis of diabetic foot syndrome. Two MMAT prototypes were developed, the most advanced version could acquire high resolution terahertz images of both feet soles in approximately 10 minutes. The terahertz images processing to map the water content in the foot sole as an objective and quantitative indicator of the skin deterioration was described. Additionally, RYG images were proposed to color-code the hydration informa-

tion for the easy visualization of high ulceration risk areas along the foot sole. A statistical analysis on the RYG-color-coded pixels was performed suggesting that the fraction of red and green pixels are potential deterioration risk indicators. In addition, a first clinical trial of the MMAT technique as diagnostic test was performed finding a correlation between the complications related to the diabetic foot syndrome (neuropathy, ulcers and amputations) and the hydration in the skin. The red and green color-coded pixels were also found to be strongly related to the deterioration in the foot of diabetic patients. Moreover, it was found that there is no correlation between ABI values and hydration of the skin suggesting that the dehydration observed in diabetic patients is due to alterations in the sympathetic nervous system which controls transpiration, rather than to a vascular problem. The sensitivity and specificity values of the MMAT technique were estimated in the range from 76% to 81% and 69% to 78%, respectively. We can therefore conclude that, this study demonstrates that the Moisture MApping by Terahertz technique has the potential to early diagnose diabetic foot syndrome by evaluating the skin hydration in the feet of diabetic patients. Yet, this technique could be further improved by performing a wider clinical trial, for example, considering young diabetic subjects to study how the skin hydration evolves with age once the disease is present. Moreover, exploring image processing and artificial intelligence techniques such as machine learning, could help in the improvement of the data analysis which might lead to better sensitivity and specificity values. Finally, given the evidence found on the relationship between neurological alteration and skin hydration, it is of interest investigating other neuropathies not related to diabetes mellitus.

Compliance with Ethical Standards

RYG-color-coded images. The protocol for measurements on human subjects presented in the RYG-color-coded images analysis derived from the proof-of-concept study was approved by the Ethics Committee of the Hospital Regional León of the Instituto de Seguridad y Servicios Sociales de los Trabajadores del Estado. All subjects signed an informed consent form.

MMAT clinical study. The MMAT clinical test was approved by the Ethics Committe of the Unidad Médica de Alta Especial (UMAE) from the Instituto Mexicano del Seguro Social (IMSS) T1 in León, Guanajuato. The volunteers were informed about the procedures and signed an informed consent form.

Bibliography

[1] W. E. Brant and C. A. Helms, *Fundamentals of diagnostic radiology*. Lippincott Williams & Wilkins, 2012.

[2] D. G. Armstrong, A. J. Boulton, and S. A. Bus, "Diabetic foot ulcers and their recurrence," *New England Journal of Medicine*, vol. 376, no. 24, pp. 2367–2375, 2017.

[3] B. A. Lipsky, A. R. Berendt, P. B. Cornia, J. C. Pile, E. J. Peters, D. G. Armstrong, H. G. Deery, J. M. Embil, W. S. Joseph, A. W. Karchmer, *et al.*, "2012 infectious diseases society of america clinical practice guideline for the diagnosis and treatment of diabetic foot infections," *Clinical infectious diseases*, vol. 54, no. 12, pp. e132–e173, 2012.

[4] S. W. Smye, J. M. Chamberlain, A. J. Fitzgerald, and E. Berry, "The interaction between terahertz radiation and biological tissue," *Physics in Medicine and Biology*, vol. 46, pp. R101–R112, aug 2001.

[5] O. Zeni, G. P. Gallerano, A. Perrotta, M. Romano, A. Sannino, M. Sarti, M. D'Arienzo, A. Doria, E. Giovenale, A. Lai, *et al.*, "Cytogenetic observations in human peripheral blood leukocytes following in vitro exposure to thz radiation: a pilot study," *Health physics*, vol. 92, no. 4, pp. 349–357, 2007.

[6] R. M. Woodward, B. E. Cole, V. P. Wallace, R. J. Pye, D. D. Arnone, E. H. Linfield, and M. Pepper, "Terahertz pulse imaging in reflection geometry of human skin cancer and skin tissue," *Physics in Medicine and Biology*, vol. 47, no. 21, p. 3853, 2002.

[7] P. C. Ashworth, E. Pickwell-MacPherson, E. Provenzano, S. E. Pinder, A. D. Purushotham, M. Pepper, and V. P. Wallace, "Terahertz pulsed spectroscopy of freshly excised human breast cancer," *Optics express*, vol. 17, no. 15, pp. 12444–12454, 2009.

[8] F. Wahaia, G. Valusis, L. M. Bernardo, A. Almeida, J. A. Moreira, P. C. Lopes, J. Macutkevic, I. Kasalynas, D. Seliuta, R. Adomavicius, *et al.*, "Detection of colon cancer by terahertz techniques," *Journal of Molecular Structure*, vol. 1006, no. 1-3, pp. 77–82, 2011.

[9] L. H. Eadie, C. B. Reid, A. J. Fitzgerald, and V. P. Wallace, "Optimizing multi-dimensional terahertz imaging analysis for colon cancer diagnosis," *Expert Systems with Applications*, vol. 40, no. 6, pp. 2043–2050, 2013.

[10] C. Yu, S. Fan, Y. Sun, and E. Pickwell-MacPherson, "The potential of terahertz imaging for cancer diagnosis: A review of investigations to date," *Quantitative Imaging in Medicine and Surgery*, vol. 2, pp. 33–45, 03 2012.

[11] Z. Taylor, R. Singh, M. Culjat, J. Suen, W. Grundfest, H. Lee, and E. Brown, "Reflective terahertz imaging of porcine skin burns," *Optics letters*, vol. 33, no. 11, pp. 1258–1260, 2008.

[12] P. Tewari, N. Bajwa, R. S. Singh, M. O. Culjat, W. S. Grundgest, Z. D. Taylor, C. P. Kealey, D. B. Bennett, K. S. Barnett, and A. Stojadinovic, "In vivo terahertz imaging of rat skin burns," *Journal of Biomedical Optics*, vol. 17, no. 4, pp. 040503–1 – 040503–3, 2012.

[13] Y.-S. Lee, *Principles of terahertz science and technology*, vol. 170. Springer Science & Business Media, 2009.

[14] R. J. Trew, "High-frequency solid-state electronic devices," *IEEE transactions on electron devices*, vol. 52, no. 5, pp. 638–649, 2005.

[15] R. Smith, "Detectors for ultraviolet, visible, and infrared radiation," *Applied Optics*, vol. 4, no. 6, pp. 631–638, 1965.

[16] D. H. Auston and M. C. Nuss, "Electrooptical generation and detection of femtosecond electrical transients," *IEEE Journal of quantum electronics*, vol. 24, no. 2, pp. 184–197, 1988.

[17] P. R. Smith, D. H. Auston, and M. C. Nuss, "Subpicosecond photoconducting dipole antennas," *IEEE Journal of Quantum Electronics*, vol. 24, no. 2, pp. 255–260, 1988.

[18] M. Bass, P. Franken, J. Ward, and G. Weinreich, "Optical rectification," *Physical Review Letters*, vol. 9, no. 11, p. 446, 1962.

[19] D. H. Auston and K. Cheung, "Coherent time-domain far-infrared spectroscopy," *JOSA B*, vol. 2, no. 4, pp. 606–612, 1985.

[20] O. Svelto and D. C. Hanna, *Principles of lasers*, vol. 1. Springer, 2010.

[21] I. Wilke, "Ho-jin song and tadao nagatsuma (eds.): Handbook of terahertz technologies: devices and applications," *Analytical and bioanalytical chemistry*, vol. 408, no. 3, p. 665, 2016.

[22] E. Pickwell-MacPherson and V. P. Wallace, "Terahertz pulsed imaging—a potential medical imaging modality?," *Photodiagnosis and Photodynamic Therapy*, vol. 6, no. 2, pp. 128–134, 2009.

[23] Z. D. Taylor, R. S. Singh, D. B. Bennett, P. Tewari, C. P. Kealey, N. Bajwa, M. O. Culjat, A. Stojadinovic, H. Lee, J.-P. Hubschman, *et al.*, "Thz medical imaging: in vivo hydration sensing," *IEEE transactions on terahertz science and technology*, vol. 1, no. 1, pp. 201–219, 2011.

[24] S. Keiding, "Dipole correlation functions in liquid benzenes measured with terahertz time domain spectroscopy," *The Journal of Physical Chemistry A*, vol. 101, no. 29, pp. 5250–5254, 1997.

[25] A. Oka and K. Tominaga, "Terahertz spectroscopy of polar solute molecules in non-polar solvents," *Journal of non-crystalline solids*, vol. 352, no. 42-49, pp. 4606–4609, 2006.

[26] P. U. Jepsen, U. Møller, and H. Merbold, "Investigation of aqueous alcohol and sugar solutions with reflection terahertz time-domain spectroscopy," *Opt. Express*, vol. 15, pp. 14717–14737, Oct 2007.

[27] P. Dutta and K. Tominaga, "Dependence of low frequency spectra on solute and solvent in solutions studied by terahertz time-domain spectroscopy," *Molecular Physics*, vol. 107, no. 18, pp. 1845–1854, 2009.

[28] Y. Yomogida, Y. Sato, R. Nozaki, T. Mishina, and J. Nakahara, "Comparative study of boson peak in normal and secondary alcohols with terahertz time-domain spectroscopy," *Physica B: Condensed Matter*, vol. 405, no. 9, pp. 2208–2212, 2010.

[29] J. A. Morales-Hernández, A. K. Singh, S. J. Villanueva-Rodriguez, and E. Castro-Camus, "Hydration shells of carbohydrate polymers studied by calorimetry and terahertz spectroscopy," *Food chemistry*, vol. 291, pp. 94–100, 2019.

[30] R. Huber, F. Tauser, A. Brodschelm, M. Bichler, G. Abstreiter, and A. Leitenstorfer, "How many-particle interactions develop after ultrafast excitation of an electron–hole plasma," *Nature*, vol. 414, no. 6861, pp. 286–289, 2001.

[31] R. Kaindl, D. Hägele, M. Carnahan, R. Lövenich, and D. Chemla, "Exciton dynamics studied via internal thz transitions," *physica status solidi (b)*, vol. 238, no. 3, pp. 451–454, 2003.

[32] R. Huber, R. A. Kaindl, B. A. Schmid, and D. S. Chemla, "Broadband terahertz study of excitonic resonances in the high-density regime in gaas/ al x ga 1- x as quantum wells," *Physical Review B*, vol. 72, no. 16, p. 161314, 2005.

[33] K. Kawase, Y. Ogawa, Y. Watanabe, and H. Inoue, "Non-destructive terahertz imaging of illicit drugs using spectral fingerprints," *Optics express*, vol. 11, no. 20, pp. 2549–2554, 2003.

[34] J. F. Federici, B. Schulkin, F. Huang, D. Gary, R. Barat, F. Oliveira, and D. Zimdars, "Thz imaging and sensing for security applications—explosives, weapons and drugs," *Semiconductor Science and Technology*, vol. 20, no. 7, p. S266, 2005.

[35] Y. Shen, a. T. Lo, P. Taday, B. Cole, W. Tribe, and M. Kemp, "Detection and identification of explosives using terahertz pulsed spectroscopic imaging," *Applied physics letters*, vol. 86, no. 24, p. 241116, 2005.

[36] A. Dobroiu, C. Otani, and K. Kawase, "Terahertz-wave sources and imaging applications," *Measurement Science and Technology*, vol. 17, no. 11, p. R161, 2006.

[37] T. Kleine-Ostmann, K. Pierz, G. Hein, P. Dawson, and M. Koch, "Audio signal transmission over thz communication channel using semiconductor modulator," *Electronics Letters*, vol. 40, no. 2, pp. 124–126, 2004.

[38] R. Piesiewicz, T. Kleine-Ostmann, N. Krumbholz, D. Mittleman, M. Koch, J. Schoebei, and T. Kurner, "Short-range ultra-broadband terahertz communications: Concepts and perspectives," *IEEE Antennas and Propagation Magazine*, vol. 49, no. 6, pp. 24–39, 2007.

[39] T. Kleine-Ostmann and T. Nagatsuma, "A review on terahertz communications research," *Journal of Infrared, Millimeter, and Terahertz Waves*, vol. 32, no. 2, pp. 143–171, 2011.

[40] H.-J. Song, K. Ajito, Y. Muramoto, A. Wakatsuki, T. Nagatsuma, and N. Kukutsu, "24 gbit/s data transmission in 300 ghz band for future terahertz communications," *Electronics Letters*, vol. 48, no. 15, pp. 953–954, 2012.

[41] Y. Monnai, K. Altmann, C. Jansen, H. Hillmer, M. Koch, and H. Shinoda, "Terahertz beam steering and variable focusing using programmable diffraction gratings," *Optics express*, vol. 21, no. 2, pp. 2347–2354, 2013.

[42] T. Nagatsuma, G. Ducournau, and C. C. Renaud, "Advances in terahertz communications accelerated by photonics," *Nature Photonics*, vol. 10, no. 6, pp. 371–379, 2016.

[43] J. M. Seifert, G. G. Hernandez-Cardoso, M. Koch, and E. Castro-Camus, "Terahertz beam steering using active diffraction grating fabricated by 3d printing," *Optics Express*, vol. 28, no. 15, pp. 21737–21744, 2020.

[44] C. L. Koch Dandolo, A. Cosentino, and P. U. Jepsen, "Inspection of panel paintings beneath gilded finishes using terahertz time-domain imaging," *Studies in Conservation*, vol. 60, no. sup1, pp. S159–S166, 2015.

[45] C. L. K. Dandolo and P. U. Jepsen, "Wall painting investigation by means of non-invasive terahertz time-domain imaging (thz-tdi): Inspection of subsurface structures buried in historical plasters," *Journal of Infrared, Millimeter, and Terahertz Waves*, vol. 37, no. 2, pp. 198–208, 2016.

[46] P. H. Siegel, "Terahertz technology in biology and medicine," *IEEE Transactions on Microwave Theory and Techniques*, vol. 52, no. 10, pp. 2438–2447, 2004.

[47] E. Castro-Camus, M. Palomar, and A. A. Covarrubias, "Leaf water dynamics of arabidopsis thaliana monitored in-vivo using terahertz time-domain spectroscopy," *Scientific Reports*, vol. 3, pp. 2910 EP –, 10 2013.

[48] L. Guo, X. Wang, P. Han, W. Sun, S. Feng, J. Ye, and Y. Zhang, "Observation of dehydration dynamics in biological tissues with terahertz digital holography," *Applied Optics*, vol. 56, no. 13, pp. F173–F178, 2017.

[49] K. Shiraga, Y. Ogawa, T. Suzuki, N. Kondo, A. Irisawa, and M. Imamura, "Characterization of dielectric responses of human cancer cells in the terahertz region," *Journal of Infrared, Millimeter, and Terahertz Waves*, vol. 35, no. 5, pp. 493–502, 2014.

[50] N. Zinov'ev, A. Fitzgerald, S. Strafford, D. Wood, F. Carmichael, R. Miles, M. Smith, and J. Chamberlain, "Identification of tooth decay using terahertz imaging and spectroscopy," in *Twenty Seventh International Conference on Infrared and Millimeter Waves*, pp. 13–14, IEEE, 2002.

[51] N. N. Zinov'ev, C. D. Sudworth, E. Berry, S. M. Strafford, D. J. Wood, F. A. Carmichael, R. E. Miles, M. A. Smith, and J. M. Chamberlain, "Identification of tooth abnormalities using terahertz imaging and spectroscopy," in *European Conference on Biomedical Optics*, p. 5141_196, Optical Society of America, 2003.

[52] B. Ferguson and X.-C. Zhang, "Materials for terahertz science and technology," *Nature materials*, vol. 1, no. 1, pp. 26–33, 2002.

[53] Y. Shen, P. Upadhya, E. Linfield, H. Beere, and A. Davies, "Ultrabroadband terahertz radiation from low-temperature-grown gaas photoconductive emitters," *Applied physics letters*, vol. 83, no. 15, pp. 3117–3119, 2003.

[54] Y. Shen, P. Upadhya, H. Beere, E. Linfield, A. Davies, I. Gregory, C. Baker, W. Tribe, and M. Evans, "Generation and detection of ultrabroadband terahertz radiation using photoconductive emitters and receivers," *Applied Physics Letters*, vol. 85, no. 2, pp. 164–166, 2004.

[55] A. Hussain and S. Andrews, "Dynamic range of ultrabroadband terahertz detection using gaas photoconductors," *Applied physics letters*, vol. 88, no. 14, p. 143514, 2006.

[56] C. Kübler, R. Huber, S. Tübel, and A. Leitenstorfer, "Ultrabroadband detection of multi-terahertz field transients with gase electro-optic sensors: Approaching the near infrared," *Applied physics letters*, vol. 85, no. 16, pp. 3360–3362, 2004.

[57] C. Kübler, R. Huber, and A. Leitenstorfer, "Ultrabroadband terahertz pulses: generation and field-resolved detection," *Semiconductor science and technology*, vol. 20, no. 7, p. S128, 2005.

[58] J. Shan, A. Nahata, and T. F. Heinz, "Terahertz time-domain spectroscopy based on nonlinear optics," *Journal of Nonlinear Optical Physics & Materials*, vol. 11, no. 01, pp. 31–48, 2002.

[59] T. D. Dorney, R. G. Baraniuk, and D. M. Mittleman, "Material parameter estimation with terahertz time-domain spectroscopy," *JOSA A*, vol. 18, no. 7, pp. 1562–1571, 2001.

[60] E. Castro-Camus and M. Johnston, "Extraction of the anisotropic dielectric properties of materials from polarization-resolved terahertz time-domain spectra," *Journal of Optics A: Pure and Applied Optics*, vol. 11, no. 10, p. 105206, 2009.

[61] J. Darrow, B. Hu, X.-C. Zhang, and D. Auston, "Subpicosecond electromagnetic pulses from large-aperture photoconducting antennas," *Optics letters*, vol. 15, no. 6, pp. 323–325, 1990.

[62] P. U. Jepsen, R. H. Jacobsen, and S. Keiding, "Generation and detection of terahertz pulses from biased semiconductor antennas," *JOSA B*, vol. 13, no. 11, pp. 2424–2436, 1996.

[63] L. Duvillaret, F. Garet, and J.-L. Coutaz, "Highly precise determination of optical constants and sample thickness in terahertz time-domain spectroscopy," *Applied optics*, vol. 38, no. 2, pp. 409–415, 1999.

[64] L. Duvillaret, F. Garet, and J.-L. Coutaz, "A reliable method for extraction of material parameters in terahertz time-domain spectroscopy," *IEEE Journal of selected topics in quantum electronics*, vol. 2, no. 3, pp. 739–746, 1996.

[65] T.-I. Jeon and D. Grischkowsky, "Characterization of optically dense, doped semiconductors by reflection thz time domain spectroscopy," *Applied Physics Letters*, vol. 72, no. 23, pp. 3032–3034, 1998.

[66] L. Thrane, R. H. Jacobsen, P. U. Jepsen, and S. Keiding, "Thz reflection spectroscopy of liquid water," *Chemical Physics Letters*, vol. 240, no. 4, pp. 330–333, 1995.

[67] C. Rønne, "Intermolecular liquid dynamics studied by thz-spectroscopy," *Aarhus University*, 2000.

[68] B. B. Hu and M. C. Nuss, "Imaging with terahertz waves," *Optics letters*, vol. 20, no. 16, pp. 1716–1718, 1995.

[69] D. M. Mittleman, R. H. Jacobsen, and M. C. Nuss, "T-ray imaging," *IEEE Journal of selected topics in quantum electronics*, vol. 2, no. 3, pp. 679–692, 1996.

[70] D. M. Mittleman, S. Hunsche, L. Boivin, and M. C. Nuss, "T-ray tomography," in *Ultrafast Electronics and Optoelectronics*, p. UF5, Optical Society of America, 1997.

[71] D. Mittleman, M. Gupta, R. Neelamani, R. Baraniuk, J. Rudd, and M. Koch, "Recent advances in terahertz imaging," *Applied Physics B*, vol. 68, no. 6, pp. 1085–1094, 1999.

[72] A. K. Singh, A. V. Pérez-López, J. Simpson, and E. Castro-Camus, "Three-dimensional water mapping of succulent agave victoriae-reginae leaves by terahertz imaging," *Scientific Reports*, vol. 10, no. 1, pp. 1–9, 2020.

[73] M. Mikerov, R. Shrestha, P. van Dommelen, D. M. Mittleman, and M. Koch, "Analysis of ancient ceramics using terahertz imaging and photogrammetry," *Optics Express*, vol. 28, no. 15, pp. 22255–22263, 2020.

[74] M. Schwerdtfeger, E. Castro-Camus, K. Krügener, W. Viöl, and M. Koch, "Beating the wavelength limit: three-dimensional imaging of buried subwavelength fractures in sculpture and construction materials by terahertz time-domain reflection spectroscopy," *Applied Optics*, vol. 52, no. 3, pp. 375–380, 2013.

[75] K. Krügener, M. Schwerdtfeger, S. F. Busch, A. Soltani, E. Castro-Camus, M. Koch, and W. Viöl, "Terahertz meets sculptural and architectural art: Evaluation and conservation of stone objects with t-ray technology," *Scientific reports*, vol. 5, no. 1, pp. 1–7, 2015.

[76] K. Krügener, S. F. Busch, A. Soltani, E. Castro-Camus, M. Koch, and W. Viöl, "Non-destructive analysis of material detachments from polychromatically glazed terracotta artwork by thz time-of-flight spectroscopy," *Journal of Infrared, Millimeter, and Terahertz Waves*, vol. 38, no. 4, pp. 495–502, 2017.

[77] K. Krügener, J. Ornik, L. M. Schneider, A. Jäckel, C. L. Koch-Dandolo, E. Castro-Camus, N. Riedl-Siedow, M. Koch, and W. Viöl, "Terahertz inspection of buildings and architectural art," *Applied Sciences*, vol. 10, no. 15, p. 5166, 2020.

[78] C. Jördens and M. Koch, "Detection of foreign bodies in chocolate with pulsed terahertz spectroscopy," *Optical Engineering*, vol. 47, no. 3, p. 037003, 2008.

[79] Y. L. Hor, J. F. Federici, and R. L. Wample, "Nondestructive evaluation of cork enclosures using terahertz/millimeter wave spectroscopy and imaging," *Applied Optics*, vol. 47, no. 1, pp. 72–78, 2008.

[80] S.-T. Han, W. K. Park, Y.-H. Ahn, W.-J. Lee, and H. S. Chun, "Development of a compact sub-terahertz gyrotron and its application to t-ray

real-time imaging for food inspection," in *2012 37th International Conference on Infrared, Millimeter, and Terahertz Waves*, pp. 1–2, IEEE, 2012.

[81] J. A. Zeitler, P. F. Taday, D. A. Newnham, M. Pepper, K. C. Gordon, and T. Rades, "Terahertz pulsed spectroscopy and imaging in the pharmaceutical setting-a review," *Journal of Pharmacy and Pharmacology*, vol. 59, no. 2, pp. 209–223, 2007.

[82] Y.-C. Shen and P. F. Taday, "Development and application of terahertz pulsed imaging for nondestructive inspection of pharmaceutical tablet," *IEEE Journal of Selected Topics in Quantum Electronics*, vol. 14, no. 2, pp. 407–415, 2008.

[83] Y.-C. Shen, "Terahertz pulsed spectroscopy and imaging for pharmaceutical applications: a review," *International journal of pharmaceutics*, vol. 417, no. 1-2, pp. 48–60, 2011.

[84] J. Jackson, M. Mourou, J. Whitaker, I. Duling Iii, S. Williamson, M. Menu, and G. Mourou, "Terahertz imaging for non-destructive evaluation of mural paintings," *Optics communications*, vol. 281, no. 4, pp. 527–532, 2008.

[85] C. L. Koch-Dandolo, T. Filtenborg, K. Fukunaga, J. Skou-Hansen, and P. U. Jepsen, "Reflection terahertz time-domain imaging for analysis of an 18th century neoclassical easel painting," *Applied optics*, vol. 54, no. 16, pp. 5123–5129, 2015.

[86] M. Inuzuka, Y. Kouzuma, N. Sugioka, K. Fukunaga, and T. Tateishi, "Investigation of layer structure of the takamatsuzuka mural paintings by terahertz imaging technique," *Journal of Infrared, Millimeter, and Terahertz Waves*, vol. 38, no. 4, pp. 380–389, 2017.

[87] C. L. K. Dandolo, G. M. P. Saldaña, M. A. I. Caballero, M. A. G. Sepúlveda, A. I. Hernández-Serrano, A. M. Orozco, J. A. Calderón, M. S. C. Zárate, K. L. González, E. C. P. de Dios, *et al.*, "Terahertz time-domain imaging to guide a conservation intervention on a stratified easel painting," *Journal of Infrared, Millimeter, and Terahertz Waves*, vol. 39, no. 8, pp. 773–784, 2018.

[88] K. Fukunaga, Y. Ogawa, S. Hayashi, and I. Hosako, "Application of terahertz spectroscopy for character recognition in a medieval manuscript," *IEICE Electronics Express*, vol. 5, no. 7, pp. 223–228, 2008.

[89] L. Öhrström, B. M. Fischer, A. Bitzer, J. Wallauer, M. Walther, and F. Rühli, "Terahertz imaging modalities of ancient egyptian mummified objects and of a naturally mummified rat," *The Anatomical Record*, vol. 298, no. 6, pp. 1135–1143, 2015.

[90] E.-M. Stübling, A. Rehn, T. Siebrecht, Y. Bauckhage, L. Öhrström, P. Eppenberger, J. C. Balzer, F. Rühli, and M. Koch, "Application of a robotic thz imaging system for sub-surface analysis of ancient human remains," *Scientific reports*, vol. 9, no. 1, pp. 1–8, 2019.

[91] F. Lambert, E. Reyes-Reyes, G. Hernandez-Cardoso, A. Gomez-Sepulveda, and E. Castro-Camus, "In situ determination of the state of conservation of paint coatings on the kiosk of guadalajara using terahertz time-domain spectroscopy," *Journal of Infrared, Millimeter, and Terahertz Waves*, vol. 41, no. 4, pp. 355–364, 2020.

[92] D. Crawley, C. Longbottom, V. P. Wallace, B. Cole, D. Arnone, and M. Pepper, "Three-dimensional terahertz pulse imaging of dental tissue," *Journal of Biomedical Optics*, vol. 8, no. 2, pp. 303–307, 2003.

[93] J. Wang, R. I. Stantchev, Q. Sun, T.-W. Chiu, A. T. Ahuja, and E. P. MacPherson, "Thz in vivo measurements: the effects of pressure on skin reflectivity," *Biomedical optics express*, vol. 9, no. 12, pp. 6467–6476, 2018.

[94] D. I. Ramos-Soto, A. K. Singh, E. Saucedo-Casas, E. Castro-Camus, and M. Alfaro-Gomez, "Visualization of moisturizer effects in stratum corneum in vitro using thz spectroscopic imaging," *Applied optics*, vol. 58, no. 24, pp. 6581–6585, 2019.

[95] M. M. Nazarov, A. P. Shkurinov, E. Kuleshov, and V. V. Tuchin, "Terahertz time-domain spectroscopy of biological tissues," *Quantum electronics*, vol. 38, no. 7, p. 647, 2008.

[96] C. Jördens, M. Scheller, B. Breitenstein, D. Selmar, and M. Koch, "Evaluation of leaf water status by means of permittivity at terahertz frequencies," *Journal of biological physics*, vol. 35, no. 3, pp. 255–264, 2009.

[97] A. Fitzgerald, E. Berry, N. Zinov'ev, S. Homer-Vanniasinkam, R. Miles, J. Chamberlain, and M. Smith, "Catalogue of human tissue optical properties at terahertz frequencies," *Journal of Biological Physics*, vol. 29, no. 2-3, pp. 123–128, 2003.

[98] E. Pickwell, B. E. Cole, A. J. Fitzgerald, M. Pepper, and V. P. Wallace, "In vivo study of human skin using pulsed terahertz radiation," *Physics in Medicine & Biology*, vol. 49, no. 9, p. 1595, 2004.

[99] I. Echchgadda, J. A. Grundt, M. Tarango, B. L. Ibey, T. D. Tongue, M. Liang, H. Xin, and G. J. Wilmink, "Using a portable terahertz spectrometer to measure the optical properties of in vivo human skin," *Journal of Biomedical Optics*, vol. 18, no. 12, p. 120503, 2013.

[100] G. G. Hernandez-Cardoso, S. C. Rojas-Landeros, M. Alfaro-Gomez, A. I. Hernandez-Serrano, I. Salas-Gutierrez, E. Lemus-Bedolla, A. R. Castillo-Guzman, H. L. Lopez-Lemus, and E. Castro-Camus, "Terahertz imaging

for early screening of diabetic foot syndrome: A proof of concept," *Scientific Reports*, vol. 7, pp. 42124 EP –, 02 2017.

[101] H. J. Liebe, G. A. Hufford, and T. Manabe, "A model for the complex permittivity of water at frequencies below 1 thz," *International Journal of Infrared and Millimeter Waves*, vol. 12, no. 7, pp. 659–675, 1991.

[102] X. C. Zeng, D. J. Bergman, P. M. Hui, and D. Stroud, "Effective-medium theory for weakly nonlinear composites," *Phys. Rev. B*, vol. 38, pp. 10970–10973, Nov 1988.

[103] J. F. Federici, "Review of moisture and liquid detection and mapping using terahertz imaging," *Journal of Infrared, Millimeter, and Terahertz Waves*, vol. 33, pp. 97–126, Feb 2012.

[104] M. Scheller, S. Wietzke, C. Jansen, and M. Koch, "Modelling heterogeneous dielectric mixtures in the terahertz regime: a quasi-static effective medium theory," *Journal of Physics D: Applied Physics*, vol. 42, p. 065415, mar 2009.

[105] M. Scheller, C. Jansen, , and M. Koch, "Applications of effective medium theories in the terahertz regime," in *Recent Optical and Photonic Technologies* (K. Y. Kim, ed.), ch. 12, Rijeka: IntechOpen, 2010.

[106] T. C. Choy, *Effective Medium Theory Principles and Applications*. Oxford Science Publications, 1999.

[107] H. Looyenga, "Dielectric constants of heterogeneous mixtures," *Physica*, vol. 31, no. 3, pp. 401–406, 1965.

[108] S. O. Nelson, "Density-permittivity relationships for powdered and granular materials," *IEEE Transactions on Instrumentation and Measurement*, vol. 54, pp. 2033–2040, Oct 2005.

[109] E. Pickwell and V. P. Wallace, "Biomedical applications of terahertz technology," *Journal of Physics D: Applied Physics*, vol. 39, pp. R301–R310, aug 2006.

[110] R. Gente, N. Born, N. Voß, W. Sannemann, J. Léon, M. Koch, and E. Castro-Camus, "Determination of leaf water content from terahertz time-domain spectroscopic data," *Journal of Infrared, Millimeter, and Terahertz Waves*, vol. 34, pp. 316–323, Apr 2013.

[111] M. Borovkova, M. Khodzitsky, P. Demchenko, O. Cherkasova, A. Popov, and I. Meglinski, "Terahertz time-domain spectroscopy for non-invasive assessment of water content in biological samples," *Biomed. Opt. Express*, vol. 9, pp. 2266–2276, May 2018.

[112] B. C. Truong, A. J. Fitzgerald, S. Fan, and V. P. Wallace, "Concentration analysis of breast tissue phantoms with terahertz spectroscopy," *Biomedical optics express*, vol. 9, no. 3, pp. 1334–1349, 2018.

[113] G. G. Hernandez-Cardoso, A. K. Singh, and E. Castro-Camus, "Empirical comparison between effective medium theory models for the dielectric response of biological tissue at terahertz frequencies," *Applied Optics*, 2020.

[114] W. H. Organization *et al.*, *Global status report on noncommunicable diseases 2014*. No. WHO/NMH/NVI/15.1, World Health Organization, 2014.

[115] T. Scully, "Diabetes in numbers," *Nature*, vol. 485, no. 7398, pp. S2–S3, 2012.

[116] A. D. Association, "Diagnosis and classification of diabetes mellitus.," *Diabetes Care*, vol. 37, no. 3, pp. 887–887, 2014.

[117] D. M. Nathan, "Long-term complications of diabetes mellitus," *New England Journal of Medicine*, vol. 328, pp. 1676–1685, 1993.

[118] H. Pham, D. G. Armstrong, C. Harvey, L. B. Harkless, J. M. Giurini, and A. Veves, "Screening techniques to identify people at high risk for diabetic foot ulceration: a prospective multicenter trial.," *Diabetes care*, vol. 23, no. 5, pp. 606–611, 2000.

[119] A. J. Boulton, L. Vileikyte, G. Ragnarson-Tennvall, and J. Apelqvist, "The global burden of diabetic foot disease," *The Lancet*, vol. 366, no. 9498, pp. 1719–1724, 2005.

[120] K. Alexiadou and J. Doupis, "Management of diabetic foot ulcers," *Diabetes Therapy*, vol. 3, no. 1, p. 4, 2012.

[121] J. A. Mayfield and J. R. Sugarman, "The use of the semmes-weinstein monofilament and other threshold tests for preventing foot ulceration and amputation in persons with diabetes," *Journal of Family Practice*, vol. 49, no. 11, pp. S17–S17, 2000.

[122] M. Edmonds, V. Roberts, and P. Watkins, "Blood flow in the diabetic neuropathic foot," *Diabetologia*, vol. 22, no. 1, pp. 9–15, 1982.

[123] G. G. Hernandez-Cardoso, S. C. Rojas-Landeros, M. Alfaro-Gomez, I. Salas-Gutierrez, and E. Castro-Camus, "Pixel statistical analysis of diabetic vs. non-diabetic foot-sole spectral terahertz reflection images," *Journal of Infrared, Millimeter, and Terahertz Waves*, 2018.

[124] K. H. Zou, A. J. O'Malley, and L. Mauri, "Receiver-operating characteristic analysis for evaluating diagnostic tests and predictive models," *Circulation*, vol. 115, no. 5, pp. 654–657, 2007.

[125] K. Hajian-Tilaki, "Receiver operating characteristic (roc) curve analysis for medical diagnostic test evaluation," *Caspian journal of internal medicine*, vol. 4, no. 2, p. 627, 2013.

[126] T. W. Rooke, A. T. Hirsch, S. Misra, A. N. Sidawy, J. A. Beckman, L. K. Findeiss, J. Golzarian, H. L. Gornik, J. L. Halperin, M. R. Jaff, *et al.*, "2011 accf/aha focused update of the guideline for the management of patients with peripheral artery disease (updating the 2005 guideline) a report of the american college of cardiology foundation/american heart association task force on practice guidelines," *Circulation*, vol. 124, no. 18, pp. 2020–2045, 2011.

[127] P. Brodal, *The central nervous system: structure and function*. Oxford University Press, 2004.

[128] K. Hajian-Tilaki, "The choice of methods in determining the optimal cut-off value for quantitative diagnostic test evaluation," *Statistical methods in medical research*, vol. 27, no. 8, pp. 2374–2383, 2018.